

The resolved star-formation relation in nearby active galactic nuclei

Viviana Casasola^{1,2}, Leslie Hunt², Françoise Combes³, and Santiago García-Burillo⁴

¹ INAF - Istituto di Radioastronomia & Italian ALMA Regional Centre, Via Gobetti 101, 40129, Bologna, Italy e-mail: casola@ira.inaf.it

² INAF - Osservatorio Astrofisico di Arcetri, Largo E. Fermi, 5, 50125, Firenze, Italy

³ Observatoire de Paris, LERMA (CNRS:UMR8112), 61 Av. de l'Observatoire, F-75014, Paris, France

⁴ Observatorio Astronómico Nacional (OAN)-Observatorio de Madrid, Alfonso XII, 3, 28014-Madrid, Spain

Received ; accepted

ABSTRACT

Aims. We present an analysis of the relation between star formation rate (SFR) surface density (Σ_{SFR}) and mass surface density of molecular gas (Σ_{H_2}), commonly referred to as the Kennicutt-Schmidt (K-S) relation, at its intrinsic spatial scale, i.e. the size of giant molecular clouds ($\sim 10\text{--}150$ pc), in the central, high-density regions of four nearby low-luminosity active galactic nuclei (AGN). These are AGN extracted from Nuclei of GALaxies (NUGA) survey. This study is aimed at investigating the correlations and slopes of the K-S relation, as a function of spatial resolution and of different ^{12}CO emission lines used to trace Σ_{H_2} , and testing its validity in the high-density central regions of spiral galaxies.

Methods. We used interferometric IRAM $^{12}\text{CO}(1\text{--}0)$ and $^{12}\text{CO}(2\text{--}1)$, and SMA $^{12}\text{CO}(3\text{--}2)$ emission line maps to derive Σ_{H_2} and $HST\text{--}H\alpha$ images to estimate Σ_{SFR} .

Results. Each galaxy is characterized by a distinct molecular SF relation at spatial scales between 20 to 200 pc. The K-S relations can be sub-linear, but also super-linear, with slopes ranging from ~ 0.5 to ~ 1.3 ; slopes are generally super-linear on spatial scales > 100 pc, and sub-linear on smaller scales. Depletion times range from ~ 1 and 2 Gyr, compatible with results for nearby normal galaxies. These findings are valid independently of which transition, $^{12}\text{CO}(1\text{--}0)$, $^{12}\text{CO}(2\text{--}1)$, or $^{12}\text{CO}(3\text{--}2)$, is used to derive Σ_{H_2} . Because of star-formation feedback, life-time of clouds, turbulent cascade, or magnetic fields, the K-S relation might be expected to degrade on small spatial scales (< 100 pc). However, we find no clear evidence for this, even on scales as small as ~ 20 pc, and this might be because of the higher density of GMCs in galaxy centers which have to resist higher shear forces. The proportionality between Σ_{H_2} and Σ_{SFR} found between 10 and $100 M_{\odot} \text{pc}^{-2}$ is valid even at high densities, $\sim 10^3 M_{\odot} \text{pc}^{-2}$. However, by adopting a common CO-to- H_2 conversion factor (α_{CO}), the central regions of the NUGA galaxies have higher Σ_{SFR} for a given gas column than those expected from the models, with a behavior that lies between the mergers/high-redshift starburst systems and the more quiescent star-forming galaxies, assuming that the first ones require a lower value of α_{CO} .

Key words. galaxies: ISM – galaxies: spiral – ISM: active – ISM: molecules – stars: formation

1. Introduction

The relationship between gas and star-formation (SF) in galaxies plays a key role in galaxy evolution. It constrains how efficiently galaxies turn their gas into stars, and also serves as essential input to simulations and models (e.g., Boissier et al. 2003; Tan et al. 1999; Springel & Hernquist 2003; Krumholz & McKee 2005). Nevertheless, despite the importance of this relationship, the processes responsible for conversion gas into stars in various galactic environments are still poorly understood.

More than fifty years ago, Schmidt (1959, 1963) suggested that the star formation rate (SFR) and the gas content in galaxies are related by:

$$\Sigma_{\text{SFR}} = A \Sigma_{\text{gas}}^N \quad (1)$$

where Σ_{SFR} and Σ_{gas} are the SFR surface density and the gas surface density, respectively, A is the normalization constant representing the efficiency of the processes regulating gas-stars conversion, and N_{fit} is the power relation index. The gas can be atomic (H I), molecular (H_2), or a combination of both ($\text{H I} + \text{H}_2$). Although the atomic phase of the interstellar medium (ISM) is directly traced by the H I emission line at 21 cm, indirect approaches are needed to estimate the distribution of H_2 . The

molecular hydrogen indeed lacks a dipole moment and typical temperatures (15–25 K) in giant molecular clouds (GMCs) are too low to excite quadrupole or vibrational transitions. For these reasons, the carbon monoxide (CO) emission lines are the most straightforward and reliable tracer of H_2 in galaxies. CO is relatively bright and its ability to trace the bulk distribution of H_2 has been confirmed via comparisons with gamma rays (Lebrun et al. 1983; Strong et al. 1988) and dust emission (Desert et al. 1988; Dame et al. 2001). Comparing the atomic gas density with the number of representative young stellar objects in the solar neighborhood Schmidt (1959) derived a power relation index $N \approx 2$ in equation (1). Values of N ranging approximately from 1.5 to 2 were further confirmed by Guibert et al. (1978), using more precise data on the radial and vertical distributions of the interstellar gas and a variety of young objects as tracers of SFR.

Later, Kennicutt (1998a,b) found that for disk averaged surface densities, both normal star-forming and starburst galaxies follow equation (1) with a power relation index of $N \approx 1.4$ for total ($\text{H I} + \text{H}_2$) gas. This correlation between gas and SFR surface density is commonly referred to as the Kennicutt-Schmidt relation (hereafter the K-S relation). Such a relation is in principle consistent with large scale gravitational instability being the major driver of dense cloud formation (Quirk 1972; Madore 1977).

Although spatially unresolved studies of HI, CO, and SFR are useful for characterizing global disk properties, understanding the mechanisms behind the SF requires resolved measurements.

It is now possible to study the K-S relation at sub-kpc scales, approaching the intrinsic scale of SF, i.e. the size of GMCs ($\sim 10\text{--}150$ pc, e.g., Solomon et al. 1987). Several factors have contributed, including the explosion in multiwavelength data for nearby galaxies (e.g., UV-GALEX: Gil de Paz et al. 2007; infrared-*Spitzer* and $H\alpha$ -*HST*: SINGS and LVL surveys, Kennicutt et al. 2003, Dale et al. 2009; far-infrared-Herschel: KINGFISH, Kennicutt et al. 2011; ^{12}CO : BIMA SONG, Helfer et al. 2003; HERACLES-IRAM 30m, Leroy et al. 2009; HI: VLA THINGS survey, Walter et al. 2008). Also technical improvements, especially the construction of millimeter interferometers, now allow higher resolution imaging of ^{12}CO in galaxies.

There is now substantial evidence that the molecular gas is well-correlated with the SFR tracers over several orders of magnitude, but mostly for regions where H_2 makes up the majority of the neutral gas, $\Sigma_{\text{H}_2} \gtrsim \Sigma_{\text{HI}}$ (e.g., Wong & Blitz 2002; Komugi et al. 2005; Kennicutt et al. 2007; Thilker et al. 2007; Schuster et al. 2007; Bigiel et al. 2008; Leroy et al. 2008; Blanc et al. 2009; Onodera et al. 2010; Verley et al. 2010; Rahman et al. 2011; Momose et al. 2013). This is because GMCs, the major reservoirs of molecular gas, are the sites of most SF in our Galaxy and other galaxies. Their properties indeed set the initial conditions for protostellar collapse and may play a role in determining the stellar initial mass function (IMF, McKee & Ostriker 2007). Moreover, it has long been known that the spatial distribution of ^{12}CO emission follows that of the stellar light and $H\alpha$ (e.g., Young & Scoville 1982; Scoville & Young 1983; Solomon et al. 1983; Tacconi & Young 1990). The lack of a clear correlation between Σ_{HI} and Σ_{SFR} inside galaxy discs (e.g., Bigiel et al. 2008) offers circumstantial evidence that SF remains coupled to the molecular, rather than total gas surface density ($\Sigma_{\text{HI}+\text{H}_2}$) even where HI makes up most of the ISM. Bigiel et al. (2008) found that Σ_{HI} saturates at surface density of $\approx 9 M_{\odot} \text{pc}^{-2}$ and gas in excess of this value is in the molecular phase of spirals and HI-dominated galaxies.

A crucial parameter in the study of the resolved K-S relation is the choice of the tracer for H_2 and SFR. In the literature, most of the studies for deriving the H_2 surface density to study the molecular SF relation are based on the $^{12}\text{CO}(1\text{--}0)$ (e.g., Rahman et al. 2011; Saintonge et al. 2011; Momose et al. 2013) or $^{12}\text{CO}(2\text{--}1)$ emission lines (e.g., Bigiel et al. 2008; Leroy et al. 2008), and more rarely on the $^{12}\text{CO}(3\text{--}2)$ transition (e.g., Komugi et al. 2007; Wilson et al. 2012). Also the dependence of the SFR on dense molecular gas mass has been explored with molecules such as HCN and HCO^+ (e.g., Gao & Solomon 2004; Wu et al. 2005; García-Burillo et al. 2012).

Over the past thirty years extensive efforts have been made to derive plausible SFRs for external galaxies (see Kennicutt 1998a; Calzetti et al. 2010, for reviews). Optical SFR tracers, such as $H\alpha$, often suffer from dust extinction which can change dramatically from location to location. Calzetti et al. (2007) found $A_V \sim 2.2$ mag in typical extragalactic HII regions and dense star-forming regions can be completely obscured with A_V that can reach ~ 6 mag (e.g., Scoville et al. 2001). In addition, the A_V value is not always known for a given galaxy. However, IR space facilities (*Spitzer* and *Herschel*) and UV (GALEX) have made it possible to also image the details of dust obscured SF.

Different SFR tracers probe different time scales and hence the SF history of any particular galaxy. $H\alpha$ emission traces ionized gas by massive ($M > 10 M_{\odot}$) stars over a timescale of < 20 Myr. The far-UV (FUV) luminosity corresponds to rela-

tively older (< 100 Myr), less massive ($\gtrsim 5 M_{\odot}$) stellar populations. The MIR $24\mu\text{m}$ emission mostly traces re-processed radiation of newborn (few Myr) OB stellar associations embedded within the parental molecular clouds. Although star clusters emerge from their natal clouds in less than 1 Myr, they remain associated with it for a much longer time scale, $\sim 10\text{--}30$ Myr, that is the time scale associated with the $24\mu\text{m}$ emission as a SFR tracer. Kennicutt et al. (2007) and Calzetti et al. (2007) have justified the feasibility of correcting the number of ionizing photons, as traced by the $H\alpha$ recombination line, for the effects of the dust extinction by adding a weighted component from the *Spitzer* MIPS $24\mu\text{m}$ luminosity in individual star-forming regions. Leroy et al. (2008) and Bigiel et al. (2008) proposed another composite SFR tracer that corrects dust attenuation of far-UV surface brightness using, also in this case, the *Spitzer* $24\mu\text{m}$ emission but with different weights. These composite SFR tracers, $H\alpha+24\mu\text{m}$ and FUV+ $24\mu\text{m}$, have been extensively used for a large number of nearby galaxies (see references above).

Spatially resolved K-S relation studies published in the last decade (e.g., Kennicutt et al. 2007; Bigiel et al. 2008; Leroy et al. 2008; Blanc et al. 2009; Bigiel et al. 2010; Eales et al. 2010; Verley et al. 2010; Bigiel et al. 2011; Liu et al. 2011; Rahman et al. 2011, 2012; Schrubba et al. 2011; Ford et al. 2013; Viaene et al. 2014) found a large spread in the value of the power relation index ($N \approx 0.6 - 3$) both within and among galaxies. For a comprehensive review on the most recent SF relation studies at sub-kpc scales we refer to Kennicutt & Evans (2012). The wide range of the value of N may be intrinsic, suggesting that different SF ‘laws’ exist, and contain valuable astrophysical information. Alternatively, it may be partially or entirely due to the adopted physical scale (e.g., Schrubba et al. 2010; Calzetti et al. 2012), the choice of the molecular gas (e.g., Krumholz & Thompson 2007; Narayanan et al. 2008) and SFR tracer, the type of galaxy under investigation, data sampling, and the fitting method used (e.g., Blanc et al. 2009; Shetty et al. 2013). In particular, different SFR tracers and spatial scales effectively sample different timescales, so that a galaxy’s SF history can play a role in determining the results of the measurements. It is also possible that these differences correspond to a spectrum of physical mechanisms present in a wide range of environments. High shear in galactic bars, harassment in a dense galaxy cluster, and galaxy mergers and interactions have the potential to either dampen or enhance the SF process (e.g., Casasola et al. 2004; Zhou et al. 2011; Lanz et al. 2013). All these environmental processes at work, both on galactic and extragalactic scales, suggests therefore that there is no universal SF relation in the Local Universe.

In addition to the slope of the empirical power relation between Σ_{gas} and Σ_{SFR} , the other crucial parameter in SF studies is the molecular gas depletion time, defined as the time needed for the present SFR to consume the existing molecular gas reservoir, $\tau_{\text{depl}} = \Sigma_{\text{gas}}/\Sigma_{\text{SFR}}$, i.e. the inverse of the star formation efficiency (SFE). One interpretation of the linear slope for the K-S relation is an approximately constant τ_{depl} , with an average τ_{depl} of about 2 Gyr in normal spirals (e.g., Leroy et al. 2013). As for the power relation index, several factors complicate the interpretation of τ_{depl} . Moreover, while a linear slope (and constant τ_{depl}) describes well the global average scaling relation in the star-forming galaxies, individual galaxies deviate from a single τ_{depl} (e.g., Saintonge et al. 2011; Leroy et al. 2013).

The objective of this paper is to explore the molecular SF relation in the inner (~ 1 kpc), high-density regions of four nearby ($D \lesssim 20$ Mpc), low-luminosity active galactic nuclei (LLAGN)

at the spatial scale of $\sim 20\text{--}200$ pc through a pixel-by-pixel analysis of the available maps. We do not discuss the correlation of SFR with the atomic component of the gas, since the gas phase is predominantly molecular in the central regions we study. These galaxies were originally part of the NUClei of GALaxies (NUGA) survey carried out at the Plateau de Bure Interferometer (PdBI, García-Burillo et al. 2003). The good spatial resolution offered by ^{12}CO NUGA observations enables us to probe GMC spatial scales around LLAGN, and better understand the SF process. Here, we investigate the correlations and slopes of the SF relation as a function of spatial resolution and of various ^{12}CO transitions (1–0, 2–1, 3–2) for deriving Σ_{H_2} , and its validity in regions with high molecular gas surface densities. The NUGA sample is ideal for such a study for several reasons: the proximity of the galaxies combined with the good spatial resolution and sensitivity afforded by PdBI and SMA and the high-resolution SFR tracers from the *Hubble Space Telescope* (*HST*) lets us probe the K-S relation on fine spatial scales that up to now have been examined only in Local Group galaxies. Moreover, the physical conditions in the NUGA LLAGN are more extreme than those found in typical spiral disks. Thus we can assess how well the warm dense gas at high column densities in AGN circumnuclear regions can form stars. These findings set the stage for what will be possible with ALMA data.

This paper is organized as follows. We describe the sample selection in Section 2, and the used data, their treatment, the procedure to derive Σ_{H_2} and Σ_{SFR} maps from the original images, and the applied fitting method in Sect. 3. In Sects. 4 and 5 we show the results on the observed relationships between Σ_{H_2} and Σ_{SFR} for individual galaxies and the whole sample, respectively. In Sect. 6 we stress the caveats and uncertainties associated with the present study, and finally in Sect. 7 we summarize our findings and give our conclusions.

2. The sample

The sample presented in this paper consists of four LLAGN selected from the NUGA survey. The NUGA project is an IRAM Plateau de Bure Interferometer (PdBI) and 30 m single-dish survey of nearby LLAGN with the aim to map, at the angular resolution of $\sim 0.5\text{--}2''$ and sensitivity of $\sim 2\text{--}4$ mJy beam $^{-1}$, the distribution and dynamics of the molecular gas through the two lowest emission lines of the ^{12}CO in the inner kpc of the galaxies, and to study the different mechanisms for gas fueling of LLAGN. Each galaxy of the core NUGA sample (12) has been studied on a case-by-case basis.

In this paper, we present the results of the study of the molecular gas spatially-resolved SF relation in the following NUGA galaxies: NGC 3627, NGC 4569, NGC 4579, and NGC 4826. This NUGA sub-sample offers heterogeneity in terms of nuclear activity, distance, detection or not of gas inflow, gas morphology, and surrounding environment. Since the sample only consists of four galaxies, the wide range of galaxy properties can not be used to infer statistical conclusions. It is worthwhile however to look at the different conditions where the SF relation is studied in the selected NUGA sub-sample. These properties are collected in Table 1. In this table, Col. (1) indicates the galaxy name, Col. (2) and (3) the coordinates of the galaxy dynamical center derived from NUGA IRAM ^{12}CO observations (see later), Col. (4) the morphological type from the Third Reference Catalog of Bright Galaxies (RC3, de Vaucouleurs et al. 1991), Col. (5) the nuclear activity, Col. (6) the distance (D), Col. (7) the inclination (i), Col. (8) the position angle (PA), Col. (9) the prevalent molecular gas morphology as detected from NUGA observations, Col. (10) the

identified molecular gas motion (i.e., inflow), Col. (11) the surrounding environment, and Col. (12) the NUGA references.

3. The data, derived parameters, and fitting method

This study is based on measurements of the molecular gas and SFR surface densities, Σ_{H_2} and Σ_{SFR} , and relies on the existence of multiwavelength datasets. We have used $^{12}\text{CO}(1\text{--}0)$, $^{12}\text{CO}(2\text{--}1)$, and $^{12}\text{CO}(3\text{--}2)$ line intensity maps to derive the surface densities of the molecular gas, and *HST* $H\alpha$ (6563 Å) emission images to estimate the surface densities of SF. In this section we describe these datasets.

3.1. IRAM $^{12}\text{CO}(1\text{--}0)$ and $^{12}\text{CO}(2\text{--}1)$ observations

$^{12}\text{CO}(1\text{--}0)$ and $^{12}\text{CO}(2\text{--}1)$ line intensity maps are part of the NUGA survey. NUGA observations have been carried out with 6 antennas of the PdBI in the ABCD configuration of the array and with the IRAM 30m single dish telescope. ^{12}CO images were reconstructed using the standard IRAM/GILDAS¹ software (Guilloteau & Lucas 2000), following the prescriptions described in García-Burillo et al. (2003), and restored with Gaussian beams. The beam sizes are typically $\lesssim 2''$ for $^{12}\text{CO}(1\text{--}0)$ and $\lesssim 1''$ for $^{12}\text{CO}(2\text{--}1)$. We used natural and uniform weightings to generate $^{12}\text{CO}(1\text{--}0)$ and $^{12}\text{CO}(2\text{--}1)$ maps, respectively. This allowed us to maximize the flux recovered in $^{12}\text{CO}(1\text{--}0)$ and optimize the spatial resolution in $^{12}\text{CO}(2\text{--}1)$. For NGC 3627 and NGC 4579 30m observations are used to compute the short spacings and complete the interferometric measurements, whereas for NGC 4569 and NGC 4826 we used ^{12}CO maps obtained only from PdBI observations.

For each NUGA galaxy we derived the position of the AGN by assuming that this coincides with the dynamical center of the galaxy (see Table 1). This choice maximizes the symmetry of the global velocity field derived from the two ^{12}CO transitions. Details on the determination of the AGN position/dynamical center are discussed on a case-by-case NUGA papers. Properties of IRAM ^{12}CO maps are collected in Table 2, and described in detail in Sect. 3.5.

3.2. SMA $^{12}\text{CO}(3\text{--}2)$ observations

For NGC 4569 and NGC 4826, we have also $^{12}\text{CO}(3\text{--}2)$ line intensity maps obtained with the Submillimeter Array (SMA) in its compact configuration with seven working antennas. $^{12}\text{CO}(3\text{--}2)$ single-dish observations carried out with the 15 m James Clerk Maxwell Telescope (JCMT) and published by Wilson et al. (2009) for NGC 4569 and Israel (2009) for NGC 4826 have been used to compute and add the missing short spacings to the SMA data. The beam sizes of $^{12}\text{CO}(3\text{--}2)$ maps are comparable with those of the IRAM $^{12}\text{CO}(1\text{--}0)$ maps, i.e. $\sim 2''$ (see Table 2). Details on these observations are contained in Boone et al. (2011).

3.3. *HST* $H\alpha$ emission-line images

We retrieved $H\alpha$ emission-line images from the Hubble Legacy Archive (HLA) that makes available *HST* WFPC2 observations of our galaxy sample. In these images, the $H\alpha$ emission line was observed through the narrow-band filters F656N or F658N, and the underlying continuum through F547N, F555W, and/or F814W (equivalent to narrow-band V , V , and I , respectively).

¹ <http://www.iram.fr/IRAMFR/GILDAS/>

Table 1: Properties of the galaxy sample.

Galaxy	α_{J2000} [^h ^m ^s]	δ_{J2000} [[°] ['] ^{''}]	RC3 type	Nuclear Act.	D [Mpc]	i [deg]	PA [deg]	Gas Morph. ^(a)	Gas Mot.	Envir.	NUGA Ref. ^(b)
(1)	(2)	(3)	(4)	(5)	(6)	(7)	(8)	(9)	(10)	(11)	(12)
NGC 3627	11 20 15.02	12 59 29.5	SAB(s)b	LINER/Seyfert 2	10.2 (1''=49 pc)	61	178	Bar	Inflow	Interacting	(1)
NGC 4569	12 36 49.80	13 09 46.3	SAB(rs)ab	Transition 2	16.8 (1''=81 pc)	62	15	Bar	Inflow	Isolated	(2,3)
NGC 4579	12 37 43.52	11 49 05.5	SAB(rs)b	LINER/Sy1.9	19.8 (1''=96 pc)	36	95	Spiral arms	Inflow	Isolated	(4,5)
NGC 4826	12 56 43.64	21 40 59.3	(R)SA(rs)ab	LINER	5.4 (1''=26 pc)	54	112	Disk	–	Isolated	(3,4,6)

Notes. ^(a) The molecular gas morphology as revealed from NUGA IRAM ¹²CO(1–0) observations. For ¹²CO(2–1) and ¹²CO(3–2) morphologies we refer to NUGA papers. ^(b) (1) Casasola et al. (2011); (2) Boone et al. (2007); (3) Boone et al. (2011); (4) García-Burillo et al. (2005); (5) García-Burillo et al. (2009); (6) García-Burillo et al. (2003).

Table 2: Basic information on ^{12}CO NUGA dataset.

Galaxy	IRAM Instrument	^{12}CO line	Beam [" \times " , $^\circ$]	1σ [Jy beam $^{-1}$ km s $^{-1}$]	F_{10}, F_{21}, F_{32} [K (Jy beam $^{-1}$) $^{-1}$]	R_{21}, R_{32}
(1)	(2)	(3)	(4)	(5)	(6)	(7)
NGC 3627	PdBI+30m	(1–0)	$2.05 \times 1.26, 30$	0.16	35.55	–
	PdBI+30m	(2–1)	$0.86 \times 0.58, 23$	0.30	46.32	0.60
NGC 4569	PdBI	(1–0)	$2.33 \times 1.46, 27$	0.25	27.00	–
	PdBI	(2–1)	$1.17 \times 0.65, 198$	0.35	30.24	0.63
	SMA+JCMT	(3–2)	$2.60 \times 2.06, -36$	6.19	1.92	0.23
NGC 4579	PdBI+30m	(1–0)	$2.03 \times 1.28, 26.03$	0.16	35.34	–
	PdBI+30m	(2–1)	$0.98 \times 0.60, -155.48$	0.32	38.94	0.90
NGC 4826	PdBI	(1–0)	2.53×1.80	0.25	20.17	–
	PdBI	(2–1)	0.77×0.55	0.36	54.21	0.67
	SMA+JCMT	(3–2)	2.58×1.94	4.44	2.05	0.38

The *HST* images have a pixel size of $0''.05$, and a spatial resolution of $0''.1$.

The available maps are emission-line-only $H\alpha$ + $[\text{NII}]$ images containing both emission from $H\alpha$ at 6563 \AA as well as $[\text{NII}]\lambda\lambda 6548, 6584 \text{ \AA}$. We removed the $[\text{NII}]$ contamination within the filter bandpass using average $[\text{NII}]/H\alpha$ values available in literature. Then, we corrected the $H\alpha$ maps both for Galactic foreground extinction and internal extinction. We assumed the values of the B -band Galactic foreground extinction $A_B(\text{Gal})$ available from the literature (see Table 3) and used the interstellar extinction curve by Cardelli et al. (1989). For three galaxies of our sample (NGC 3627, NGC 4569, and NGC 4826), internal extinction corrections have been extracted from Calzetti et al. (2007) using $\text{Pa}\alpha$ images as a yardstick for calibrating the MIR emission. The hydrogen emission lines trace the number of ionizing photons, and the $\text{Pa}\alpha$ line (at $1.8756 \mu\text{m}$) is only modestly impacted by dust extinction. Because of its relative insensitivity to dust extinction (less than a factor 2 of correction for typical extinction in nearby galaxies, $A_V \lesssim 5 \text{ mag}$, Calzetti et al. 2007), $\text{Pa}\alpha$ is a nearly unbiased tracer of the current SFR (Kennicutt 1998b). Among the various SFR calibrations, the linear combination of the observed $H\alpha$ and the $24 \mu\text{m}$ emission is the one most tightly correlated with the extinction-corrected $\text{Pa}\alpha$ emission (Calzetti et al. 2007). The most straightforward interpretation of this trend is that the $24 \mu\text{m}$ emission traces the dust obscured SF, while the observed $H\alpha$ emission traces the unobscured one (Kennicutt et al. 2007). Thus, the combination of the two recovers all the SF in a given region. This interpretation is confirmed by models (e.g., STARBURST99, 2005 update, Leitherer et al. 2005; Draine & Li 2007), which also suggest the trend to be relatively independent of the characteristics of the underlying star-forming population. This implies that $H\alpha/\text{Pa}\alpha$ ratio and the internal extinction derived from it, for instance $A_V(\text{int})$ in the V -band as performed by Calzetti et al. (2007), is a good tracer of the internal extinction of a galaxy.

For NGC 4579, rather than the $H\alpha/\text{Pa}\alpha$ ratio, we used the internal extinction derived from the Balmer decrement by Ho (1999). One of the most reliable techniques to estimate interstellar extinction is indeed to measure the flux ratio of two nebular Balmer emission lines such as $H\alpha/H\beta$ (i.e., the Balmer decrement). The determination of dust extinction from the Balmer decrement has been shown to be a very successful technique in the Local Universe since the first statistical work by Kennicutt (1992). These results have been improved upon by the large amount of optical spectra provided by the Sloan Digital Sky Survey (SDSS), which were analyzed in this context by Brinchmann et al. (2004) and Garn & Best (2010). The main limitation to apply the internal extinction correction derived from Balmer decrement is to neglect a possible completely obscured SFR component, and hence to underestimate the total SFR. In any case, NGC 4579 has a $A_V(\text{int})$ value similar to those of the other galaxies, as shown in Table 3. This table collects the properties of the original $H\alpha$ + $[\text{NII}]$ images and the values of the parameters used to obtain final $H\alpha$ maps. In Table 3, Col. (1) indicates the galaxy name, Col. (2) the *HST* instrument, Col. (3) the 1σ noise of the background subtracted $H\alpha$ + $[\text{NII}]$ images, Col. (4) the adopted $[\text{NII}]/H\alpha$ ratio, Col. (5) the B -band Galactic foreground extinction $[A_B(\text{Gal})]$, and Col. (6) the V -band internal extinction $[A_V(\text{int})]$.

3.4. Image treatment

With the images described above, we constructed maps of Σ_{H_2} and Σ_{SFR} to perform a pixel-by-pixel analysis of the spatially resolved K-S relation. The procedures to obtain the final maps are described later, in Sections 3.5 and 3.6. Since we compared images with different properties and large spread in resolution, the first task was to convert them to a common alignment and resolution.

All the original images ($^{12}\text{CO}(1-0)$, $^{12}\text{CO}(2-1)$, $^{12}\text{CO}(3-2)$, and $H\alpha$) have been centered on the dynamical centers of the galaxies derived from NUGA IRAM ^{12}CO observations (see Table 1). The $H\alpha$ maps have been convolved to the resolution of the ^{12}CO (1-0, 2-1, and 3-2) maps, with a Gaussian beam (on the sky), i.e., we do not account for the inclination of the galaxy. Then, all maps have been re-sampled to a pixel size equal to the adopted ^{12}CO resolution (see for instance Vutisalchavakul et al. 2014, for a similar treatment of images). Since the spatial resolution and pixel size are equivalent, the pixels can be considered as roughly statistically independent, and there should be little correlation among them. Each pixel was thus treated as a single data point. Finally, we have also convolved all maps to a common 200 pc resolution in order to be able to distinguish between effects due to different J transitions and spatial resolution. These procedures have been performed by using IRAM/GILDAS and IRAF² softwares.

We thus probe the gas and SFR surface densities in individual galaxies on physical scales ranging from 17 pc to 190 pc, as well as with a common resolution of 200 pc. Such scales are smaller than those previously scrutinized outside the Local Group (e.g., Bigiel et al. 2008; Leroy et al. 2008; Rahman et al. 2011), and are superior in this respect to other kinds of analyses, such as azimuthally averaged radial profiles (e.g., Kennicutt 1989; Bigiel et al. 2008; Rahman et al. 2011) or the aperture analysis encompassing star forming regions and centering on $H\alpha$ emission peaks (e.g., Kennicutt et al. 2007; Blanc et al. 2009).

3.5. Molecular gas surface density maps

The availability of $^{12}\text{CO}(1-0)$, $^{12}\text{CO}(2-1)$, and $^{12}\text{CO}(3-2)$ data offers Σ_{H_2} maps at different resolutions and the possibility to compare the three lowest ^{12}CO transitions in terms of the K-S relation.

We derived Σ_{H_2} maps from $^{12}\text{CO}(1-0)$, $^{12}\text{CO}(2-1)$, and $^{12}\text{CO}(3-2)$ integrated intensity maps ($S_{\text{CO}(1-0)}$, $S_{\text{CO}(2-1)}$, $S_{\text{CO}(3-2)}$) by adopting a constant value for the X_{CO} conversion factor, $X_{\text{CO}} = 2.2 \times 10^{20} \text{ cm}^{-2} (\text{K km s}^{-1})^{-1}$ (Solomon & Barrett 1991) that corresponds to $\alpha_{\text{CO}} = 3.5 M_{\odot} \text{ pc}^{-2} (\text{K km s}^{-1})^{-1}$ (e.g., Narayanan et al. 2012; Bolatto et al. 2013). For $^{12}\text{CO}(1-0)$ emission, the conversion to Σ_{H_2} is:

$$\Sigma_{\text{H}_2} = 3.5 S_{\text{CO}(1-0)} F_{10} \cos i \quad (2)$$

where Σ_{H_2} is in units of $M_{\odot} \text{ pc}^{-2}$, $S_{\text{CO}(1-0)}$ in $\text{Jy beam}^{-1} \text{ km s}^{-1}$, F_{10} is the conversion factor from flux density to brightness temperature for the $^{12}\text{CO}(1-0)$ line in $\text{K} (\text{Jy beam}^{-1})^{-1}$, and i is the galaxy inclination. For $^{12}\text{CO}(2-1)$ emission, the conversion to Σ_{H_2} is derived from equation (2) by defining R_{21} as the $^{12}\text{CO}(2-1)$

² IRAF is the Image Reduction and Analysis Facility. IRAF is written and supported by the National Optical Astronomy Observatories (NOAO) in Tucson, Arizona. NOAO is operated by the Association of Universities for Research in Astronomy (AURA), Inc. under cooperative agreement with the National Science Foundation

Table 3: Basic information on *HST*-H α dataset.

Galaxy	<i>HST</i> Instrument	1σ [erg s $^{-1}$ cm $^{-2}$]	[NII]/H α	A_B (Gal) [mag]	A_V (int) [mag]
(1)	(2)	(3)	(4)	(5)	(6)
NGC 3627	WFPC2(F658N)	5.43×10^{-19}	0.54 ^(a)	0.08 ^(a)	1.94 ^(b)
NGC 4569	WFPC2(F656N)	1.90×10^{-18}	0.50 ^(b)	0.20 ^(c)	1.05 ^(b)
NGC 4579	WFPC2(F658N)	9.49×10^{-18}	0.62 ^(d)	0.18 ^(c)	2.10 ^(e)
NGC 4826	WFPC2(F656N)	6.19×10^{-18}	0.51 ^(a)	0.16 ^(a)	1.97 ^(b)

Notes. ^(a) Kennicutt et al. (2008). These values are an average of the values from the maps of Burstein & Heiles (1982) and Schlegel et al. (1998). ^(b) Calzetti et al. (2007). ^(c) From NED. ^(d) Kennicutt et al. (2009). ^(e) Ho (1999).

1)/ $^{12}\text{CO}(1-0)$ line ratio in temperature units:

$$\Sigma_{\text{H}_2} = 3.5 \frac{S_{\text{CO}(2-1)}}{R_{21}} F_{21} \cos i \quad (3)$$

where F_{21} is the conversion factor from flux density to brightness temperature for the $^{12}\text{CO}(2-1)$ line. Consistently with equation (3), for $^{12}\text{CO}(3-2)$ emission the conversion to Σ_{H_2} is derived by defining R_{32} as the $^{12}\text{CO}(3-2)/^{12}\text{CO}(1-0)$ line ratio:

$$\Sigma_{\text{H}_2} = 3.5 \frac{S_{\text{CO}(3-2)}}{R_{32}} F_{32} \cos i \quad (4)$$

where F_{32} is the conversion factor from flux density to brightness temperature for the $^{12}\text{CO}(3-2)$ line. Both R_{21} and R_{32} used in the equations (3) and (4), respectively, have been measured for each NUGA galaxy; we use the mean value of these measured ratios to convert all transitions to CO(1-0). Equations (2), (3), and (4) define *hydrogen* surface densities; i.e., they do not include any contribution from helium. To scale our quoted surface densities to account for helium, they should be multiplied by a factor ~ 1.36 .

The values needed to apply equations (2), (3), and (4) are listed in Tables 1 and 2. In Table 2, Col. (1) gives the galaxy name; Col. (2) the instruments used for observations; Col. (3) the observed ^{12}CO transition; Col. (4) the Gaussian beam FWHM; Col. (5) the 1σ noise of the image; Col. (6) the conversion factor from flux density to brightness temperature for the three ^{12}CO transitions, and Col. (7) the R_{21} and R_{32} line ratios.

3.6. Star formation rate surface density maps

Several SFR calibrations using different tracers, based on a variety of galaxy and/or region samples and stellar IMFs, have been published (e.g., Wu et al. 2005; Calzetti et al. 2007; Zhu et al. 2008; Rieke et al. 2009). As stated above, the H α recombination emission line provides a nearly instantaneous measure of the SFR independently of the previous SF history. Among the hydrogen recombination lines, H α is the most widely used as SFR tracer because of its higher intensity and lower sensitivity to dust attenuation than bluer nebular lines (e.g., Ly α , Ly β , H β).

To derive SFR maps we used the conversion between SFR and dust extinction-corrected H α flux density derived by Calzetti et al. (2007):

$$\Sigma_{\text{SFR}} = 5.3 \times 10^{-42} S(\text{H}\alpha)_{\text{corr}} \cos i \quad (5)$$

where Σ_{SFR} is in units of $\text{M}_{\odot} \text{yr}^{-1} \text{kpc}^{-2}$, and $S(\text{H}\alpha)_{\text{corr}}$ is the dust extinction-corrected H α in $\text{erg s}^{-1} \text{kpc}^{-2}$. This calibration has been derived assuming the stellar IMF of STARBURST99,

which consists of two power laws, with slope -1.3 in the range $0.1-0.5 \text{M}_{\odot}$ and slope -2.3 in the range $0.5-120 \text{M}_{\odot}$ (for details on the adopted models of stellar populations see Appendix A2 in Calzetti et al. 2007).

We have also checked that the H α emission is uncontaminated by emission from the AGN by comparing different (albeit lower resolution) estimators of SFR. There is virtually no contamination from AGN-excited H α emission outside the central pixel for NGC 3627 and NGC 4826. Although NGC 4826 has no X-ray source and NGC 3627 is only weakly detected (Hernández-García et al. 2013), NGC 4569 and NGC 4579 both have weak nuclear X-ray sources (Dudik et al. 2005). In NGC 4579 potential AGN contamination may be more of a problem because of the broad H α emission (Ho et al. 1997). Nevertheless, the SFR inferred from broad H α is $\sim 0.02 \text{M}_{\odot} \text{yr}^{-1}$, while the total SFR for this galaxy is $\sim 2.2 \text{M}_{\odot} \text{yr}^{-1}$ (see Table 6), more than 100 times larger. Hence, we conclude that star formation processes are dominating over the AGN in our sample galaxies. In any case, for safety, in NGC 4569 and NGC 4579 we have masked the central 2×2 pixels since there was the possibility that the strong H α emission there is due to the AGN.

3.7. Fitting method

With the images described above, we constructed maps of Σ_{H_2} and Σ_{SFR} to perform a pixel-by-pixel analysis of the spatially resolved K-S relation. We used data above 3σ significance both in Σ_{H_2} and Σ_{SFR} maps.

We fitted the data in logarithmic space:

$$\log(\Sigma_{\text{SFR}}) = A_{\text{fit}} + N_{\text{fit}} \times \log(\Sigma_{\text{H}_2}) \quad (6)$$

where A_{fit} is the intercept and N_{fit} is the index of the K-S relation. We use the Ordinary Least Squares (OLS) linear bisector method (Isobe et al. 1990; Feigelson & Babu 1992), adopted in several SF relation studies (e.g., Bigiel et al. 2008; Schrubba et al. 2011; Momose et al. 2013).

For statistical completeness, we also give results derived from a robust regression fitting method (Li 1985; Fox 1997), an alternative to least squares regression which provides increased uncertainties of slopes and intercepts with respect to those given by the OLS bisector method. These fits are implemented in the public-domain statistical software package *R* (Ihaka & Gentleman 1996). However, in the following, we present and discuss results emerging from the OLS bisector method for reasons described later in Sect. 6.3.

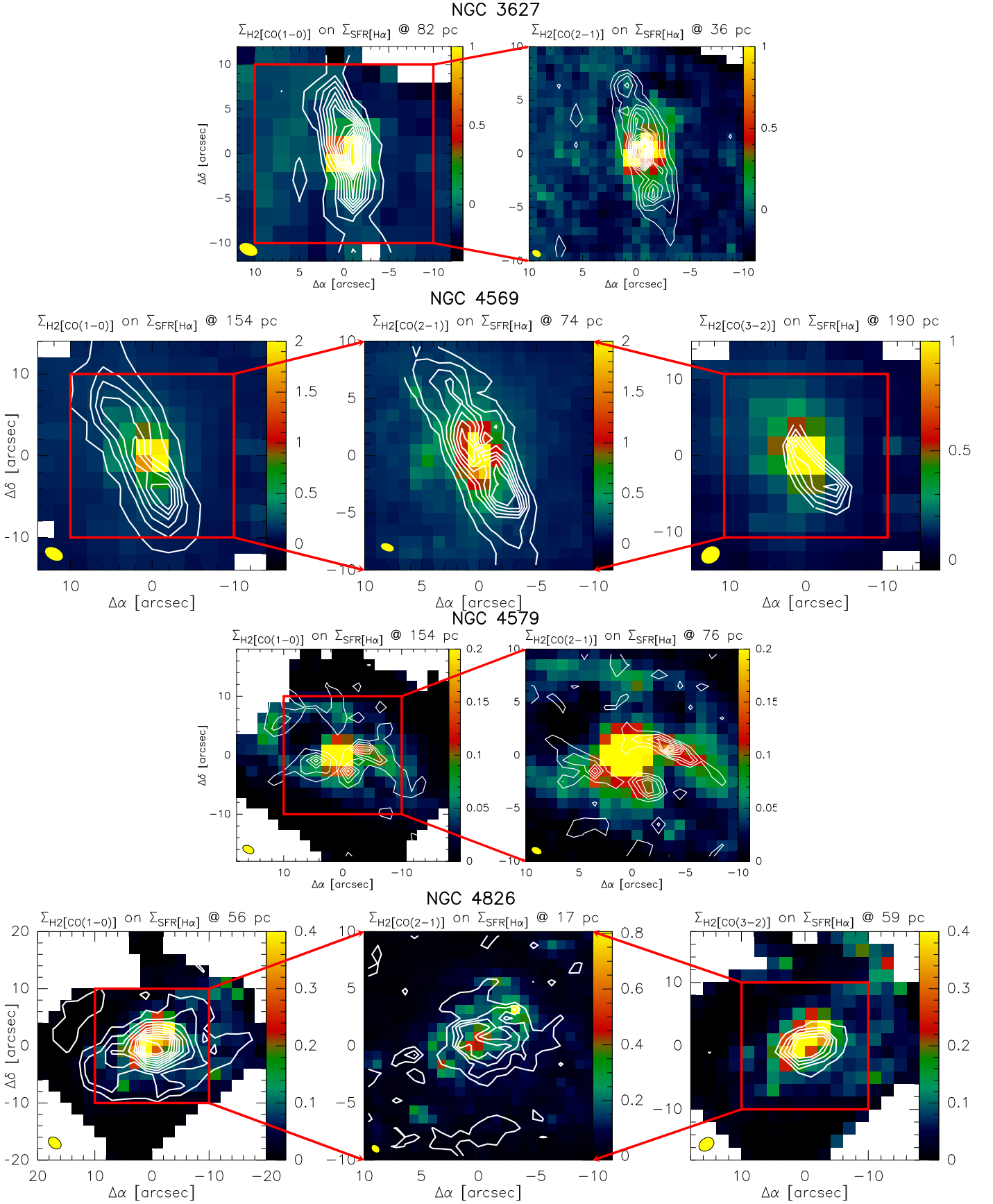


Fig. 1: Σ_{H_2} contours in $\text{M}_{\odot} \text{pc}^{-2}$ derived from $^{12}\text{CO}(1-0)$, $^{12}\text{CO}(2-1)$, and $^{12}\text{CO}(3-2)$ are overlaid on Σ_{SFR} images in $\text{M}_{\odot} \text{yr}^{-1} \text{kpc}^{-2}$ at the intrinsic spatial resolution of the ^{12}CO data and with pixel sizes equal to the ^{12}CO resolution. The beams are plotted (in yellow) in the lower left corners of maps and their values are listed in Table 2. $(\Delta\alpha, \Delta\delta)$ -offsets are with respect to the dynamical center of each galaxy. Σ_{H_2} contours are drawn starting from noise levels $>3\sigma$ with contour spacings that are whole multiples of $>3\sigma$.

4. The molecular star formation relation for individual galaxies

In this section we present the results obtained by the study of the pixel-by-pixel molecular K-S relation for each galaxy of our sample, using the two/three lowest ^{12}CO transitions for deriving Σ_{H_2} and $\text{H}\alpha$ emission for Σ_{SFR} , with spatial resolution ranging from ~ 20 to 200 pc. For every galaxy we show two sets of figures. The first one (Fig. 1) displays overlays of Σ_{H_2} contours (above 3σ) in $\text{M}_\odot \text{pc}^{-2}$ derived from $^{12}\text{CO}(1-0)$, $^{12}\text{CO}(2-1)$, and $^{12}\text{CO}(3-2)$ emission line on Σ_{SFR} maps in $\text{M}_\odot \text{yr}^{-1} \text{kpc}^{-2}$ derived from $\text{H}\alpha$ emission line at the resolution of original ^{12}CO data. The images involved in these overlays have been obtained following prescriptions described in Sects. 3.4, 3.5, and 3.6. Each panel of Fig. 1 reports the galaxy name, the reference to the ^{12}CO emission line used to derive Σ_{H_2} , and the spatial resolution under analysis, i.e. that offered by the intrinsic ^{12}CO line map and at which the $\text{H}\alpha$ image has been degraded. The second set of images (Figs. 2–6) consists of two or three plots for galaxy, according to the available ^{12}CO line maps, displaying the K-S relation at the intrinsic resolution of the ^{12}CO line data. These plots contain the galaxy name, the reference to the adopted ^{12}CO line for deriving Σ_{H_2} , the spatial resolution, the fit line derived from the OLS bisector method described in Sect. 3.7, the values of the power index N_{fit} and of the intercept A_{fit} and their uncertainties of the fit line according to equation (6), and the derived value for τ_{depl} defined as $\tau_{\text{depl}} \equiv \langle \Sigma_{\text{H}_2} \rangle / \langle \Sigma_{\text{SFR}} \rangle$ (e.g., Leroy et al. 2013).

The available FoVs vary as a function of observed line and instrument. IRAM $^{12}\text{CO}(1-0)$ maps have a FoV of the primary beam of $\sim 42''$, IRAM $^{12}\text{CO}(2-1)$ of $\sim 21''$, SMA $^{12}\text{CO}(3-2)$ of $\sim 36''$, while *HST* $\text{H}\alpha$ images have usable FoVs ranging from $\sim 24''$ to $\sim 40''$.

The results of this analysis, including the findings derived convolving all maps to the common spatial resolution of 200 pc, are collected in Table 4. In this table, Col. (1) indicates the galaxy name; Col. (2) the ^{12}CO transition used to derive Σ_{H_2} ; Col. (3) the spatial resolution in pc; Col. (4) the available FoV (diameter) in arcsec on the plane of the sky; Col. (5) the radius under investigation in kpc on the plane of the galaxy; Cols. (6) and (7) the power index ($N_{\text{fit(OLS bis.)}}$) and the intercept ($A_{\text{fit(OLS bis.)}}$) and their uncertainties of the OLS bisector fitting line (for simplicity in the text these two parameters are indicated with N_{fit} and A_{fit}); Col. (8) the Pearson correlation coefficient ($r_{\text{corr(OLS bis.)}}$) of the OLS bisector fitting line (for simplicity in the text indicated with r_{corr}) and the number of points under analysis (n. pts); Cols. (9) and (10) the power index ($N_{\text{fit(RR)}}$) and the intercept ($A_{\text{fit(RR)}}$) and their uncertainties of the robust regression fitting line; Col. (11) the mean Σ_{H_2} ($\langle \Sigma_{\text{H}_2} \rangle$) in $\text{M}_\odot \text{pc}^{-2}$ within the FoV and taking into account only data points above 3σ significance; Col. (12) the mean Σ_{SFR} ($\langle \Sigma_{\text{SFR}} \rangle$) in $\text{M}_\odot \text{yr}^{-1} \text{kpc}^{-2}$ under the same conditions; Col. (13) the molecular τ_{depl} in Gyr; and Col. (14) the final pixel size of ^{12}CO and $\text{H}\alpha$ images after procedures described in Sect. 3.4.

4.1. NGC 3627

NGC 3627 (Messier 66) is an interacting (e.g., Casasola et al. 2004) and barred galaxy classified as SAB(s)b at a distance of 10 Mpc, with signatures of a LINER/Seyfert 2 type nuclear activity (Ho et al. 1997). With NGC 3623 and NGC 3628, it forms the well-known Leo Triplet (M 66 Group, VV 308). Optical broad-band images of NGC 3627 reveal a pronounced and asymmetric spiral pattern with heavy dust lanes, indicating strong density wave action (Ptak et al. 2006). While the

western arm is accompanied by weak traces of SF visible in $\text{H}\alpha$, the eastern arm contains a star-forming segment in its inner part (Smith et al. 1994; Chemin et al. 2003). NGC 3627 also possesses X-ray properties of a galaxy with a recent starburst (Dahlem et al. 1996). Both the radio continuum (2.8 cm and 20 cm, Urbanik et al. 1985; Paladino et al. 2008) and the CO emissions (e.g., Regan et al. 2001; Paladino et al. 2008; Haan et al. 2009; Casasola et al. 2011; Watanabe et al. 2011) show a nuclear peak, extending along the leading edges of the bar forming two broad maxima at the bar ends, and then the spiral arms trail off from the bar ends. On the contrary, the $\text{H}\alpha$ emission exhibits a spiral morphology without signatures of a bar in the atomic gas (Haan et al. 2008; Walter et al. 2008). The derived gravity torque budget shows that NGC 3627 is a potential *smoking gun* of inner gas inflow at a resolution of ~ 60 pc (Casasola et al. 2011). In addition to ^{12}CO lines, other molecular transitions have been detected in NGC 3627, including $\text{HCN}(1-0)$, $\text{HCN}(2-1)$, $\text{HCN}(3-2)$, $\text{HCO}^+(1-0)$, and $\text{HCO}^+(3-2)$, suggesting the presence of high density gas (e.g., Gao & Solomon 2004; Krips et al. 2008).

The panels of the first line of Fig. 1 show the superposition of Σ_{H_2} image contours derived from $^{12}\text{CO}(1-0)$ and $^{12}\text{CO}(2-1)$ emission lines overlaid on Σ_{SFR} images estimated from the $\text{H}\alpha$ emission at the intrinsic resolutions of CO maps, i.e., $\sim 1''.7$ (~ 82 pc) for the (1–0) transition and $\sim 0''.7$ (~ 36 pc) for the (2–1) one. Σ_{H_2} has been derived from $^{12}\text{CO}(1-0)$ and $^{12}\text{CO}(2-1)$ emission lines by using Eqs. (2) and (3), respectively, and Σ_{SFR} by using Eq. (5). For $^{12}\text{CO}(1-0)$ (left panel), the Σ_{H_2} and Σ_{SFR} peaks are spatially coincident in the limit of the resolution of $\sim 1''.7$ and the two distributions are quite consistent within a radius of $\sim 3-4''$ (150–200 pc) from the nucleus (on the plane of the sky). At larger distances, Σ_{H_2} and Σ_{SFR} are not correlated, mainly because Σ_{SFR} is not distributed along a bar as is Σ_{H_2} . Similar (anti-)correlations also characterize the comparison between Σ_{H_2} derived from $^{12}\text{CO}(2-1)$ emission line and Σ_{SFR} at the resolution of $\sim 0''.7$ (right panel).

The left panel of Fig. 2 shows the molecular K-S relation derived for NGC 3627 using the $^{12}\text{CO}(1-0)$ emission line to estimate Σ_{H_2} at the resolution of 82 pc. At this resolution the power index N_{fit} is equal to 1.18 ± 0.11 within a radius of 1.3 kpc (on the plane of the galaxy). Following the same procedure but convolving the original $^{12}\text{CO}(1-0)$ and $\text{H}\alpha$ maps at the lower resolution of 200 pc, the K-S relation has N_{fit} equal to 1.11 ± 0.41 . The right panel of Fig. 2 shows the results obtained using the $^{12}\text{CO}(2-1)$ emission line to derive Σ_{H_2} (Eq. 3) at the resolution of 36 pc. At this resolution $N_{\text{fit}} = 1.16 \pm 0.05$ within a radius of 1.1 kpc (on the plane of the galaxy), while N_{fit} increases to 1.59 ± 0.63 at the resolution of 200 pc. Although all the derived N_{fit} values are consistent with literature results (see later discussion in Sect. 5.1), the K-S relations studied at the resolution of 200 pc -for both $^{12}\text{CO}(1-0)$ and $^{12}\text{CO}(2-1)$ emission lines- with only four data points involved in the analysis do not allow us to infer statistical conclusions. In NGC 3627, we can only say that $N_{\text{fit}} \sim 1.2$ both with Σ_{H_2} derived from $^{12}\text{CO}(1-0)$ at 82 pc and from $^{12}\text{CO}(2-1)$ at 36 pc.

Neglecting the 200 pc-resolution cases, the Pearson correlation coefficient is $\sim 0.6 - 0.7$ and τ_{depl} is $\sim 1.2 - 1.3$ Gyr for both the lowest ^{12}CO transitions.

4.2. NGC 4569

NGC 4569 (Messier 90) is a bright SAB(rs)ab galaxy at a distance of 17 Mpc in the Virgo Cluster. A large scale bar is seen

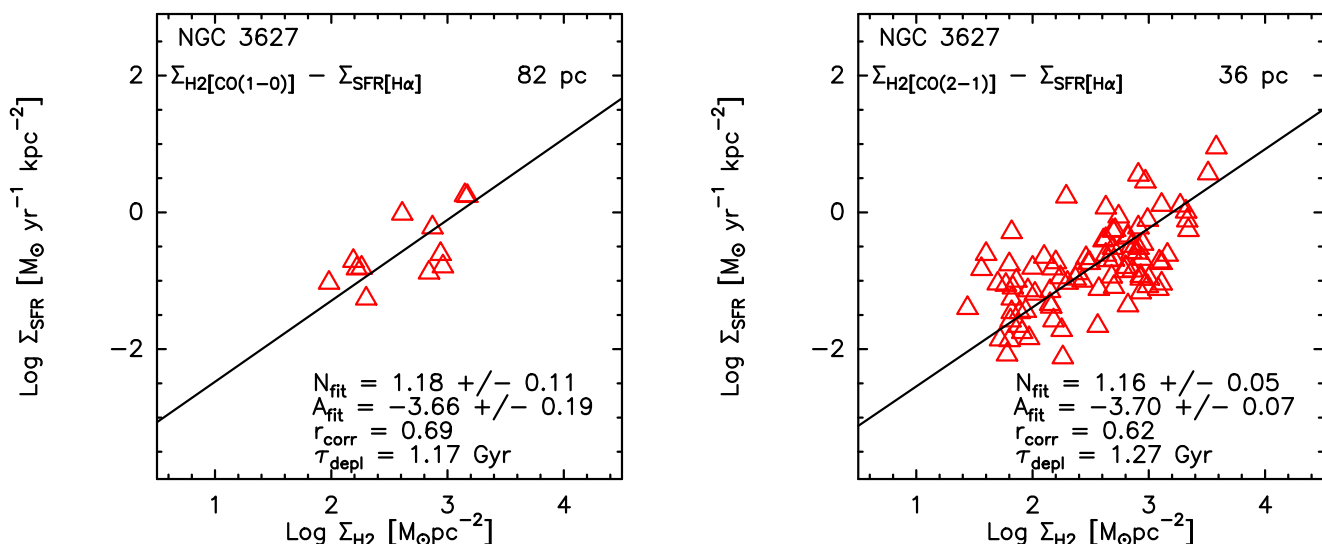


Fig. 2: *Left panel:* The K-S relation plot for NGC 3627 at the resolution of 82 pc. Σ_{H_2} has been derived from the $^{12}\text{CO}(1-0)$ emission line map and Σ_{SFR} from the $\text{H}\alpha$ image based on equations (2) and (5), respectively. Red triangles indicate data points above 3σ significance both in Σ_{H_2} and Σ_{SFR} , within a radius of 1.3 kpc (on the plane of the galaxy). The solid black line indicates the OLS bisector fitting line (see Sect. 3.7 for fitting method). The index N_{fit} and the intercept A_{fit} of the OLS bisector fitting line, the Pearson correlation coefficient r_{core} , and τ_{depl} values are reported in figure. *Right panel:* Same as left panel with Σ_{H_2} derived from the $^{12}\text{CO}(2-1)$ emission line map based on equation (3) at the resolution of 36 pc. Red triangles indicate data points above 3σ significance both in Σ_{H_2} and Σ_{SFR} , within a radius of 1.1 kpc (on the plane of the galaxy).

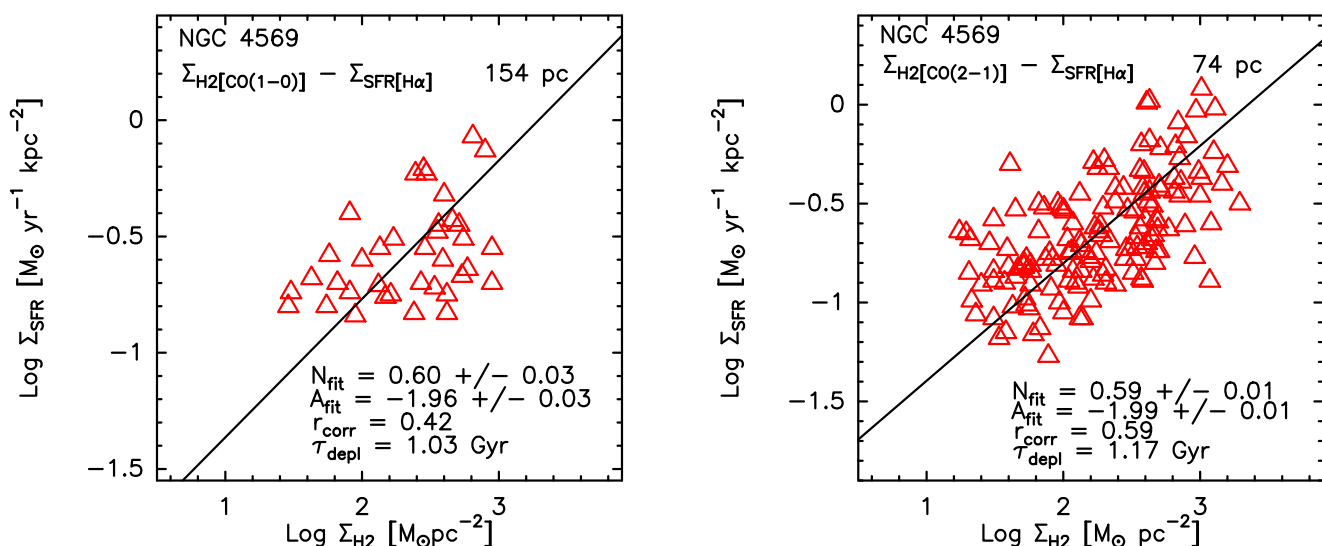


Fig. 3: *Left panel:* Same as left panel of Fig. 2 for NGC 4569 at the resolution of 154 pc. Red triangles indicate data points above 3σ significance both in Σ_{H_2} and Σ_{SFR} , within a radius of 2.9 kpc (on the plane of the galaxy). *Right panel:* Same as left panel with Σ_{H_2} derived from the $^{12}\text{CO}(2-1)$ emission line map at the resolution of 74 pc. Red triangles indicate data points above 3σ significance both in Σ_{H_2} and Σ_{SFR} , within a radius of 2.1 kpc (on the plane of the galaxy).

in NIR images (Laurikainen & Salo 2002) and is almost aligned with the major axis of the galaxy (PA = 15 deg according to Jogee et al. 2005). The galaxy harbors a nucleus of the transition type (type T2 in Ho et al. 1997) which exhibits a pronounced nuclear starburst activity. H α emission line observations have revealed that in NGC 4569 the atomic gas is distributed along a central bar with radius of $\sim 60''$ (~ 5 kpc, Haan et al. 2008). Interferometric CO observations of NGC 4569 presented previously (e.g., Helfer et al. 2003; Jogee et al. 2005; Nakanishi et al. 2005; Boone et al. 2007) have shown that the major part of the molecular gas detected in the inner $20''$ is concentrated within a radius

of 800 pc, distributed along the large scale stellar bar seen in NIR observations, and with a peak close to the center and another one at ~ 500 pc from it. A hole in the CO distribution coincides with the nucleus where most of the H α emission and blue light are emitted (Pogge et al. 2000). Boone et al. (2007) have also demonstrated that the gravitational torques are able to efficiently funnel the gas down to ~ 300 pc.

The panels of the second line of Fig. 1 show the comparison between Σ_{H_2} and Σ_{SFR} distributions in NGC 4569 at resolutions of $\sim 1''.9$ (~ 154 pc from $^{12}\text{CO}(1-0)$), $\sim 0''.9$ (~ 74 pc from $^{12}\text{CO}(2-1)$), and $\sim 2''.3$ (~ 190 pc from $^{12}\text{CO}(3-2)$). The case involving the

$^{12}\text{CO}(3-2)$ emission line refers to Eq. (4) for deriving Σ_{H_2} . From these overlays it can be seen that Σ_{H_2} and Σ_{SFR} are differently distributed at the available resolutions. While Σ_{SFR} is centrally concentrated and peaked, Σ_{H_2} (derived both from $^{12}\text{CO}(1-0)$ and $^{12}\text{CO}(2-1)$ emission line) is distributed along a large scale bar of $\sim 17'' \times 6''$ ($\sim 1.4 \text{ kpc} \times 0.5 \text{ kpc}$) in size (in the plane of the sky) whose peak is far away from the peak of Σ_{SFR} . The same distribution is also visible in the SMA $^{12}\text{CO}(3-2)$ map. There are, however, differences, perhaps due to the lower S/N ratio of the $^{12}\text{CO}(3-2)$ SMA data relative to the IRAM observations (Boone et al. 2011).

Similarly to NGC 3627, NGC 4569 exhibits a centrally concentrated morphology in the Σ_{SFR} images and a bar-like distribution in the Σ_{gas} maps. This could mean that the action of the bar has transported the gas to the nuclear regions to fuel a mini-starburst episode as found in many nearby spiral galaxies (Sakamoto et al. 1999).

Figure 3 and the left panel of Fig. 6 show the molecular K-S relation derived for NGC 4569 with Σ_{H_2} estimated from the three lowest ^{12}CO emission lines at the intrinsic resolution of the ^{12}CO maps. These figures together with findings collected in Table 4 show that NGC 4569 has an index N_{fit} of the K-S relation that is sub-linear ($\sim 0.6 - 0.7$) for the three available ^{12}CO transitions studied at spatial scales from 74 to 200 pc (producing six sub-cases), roughly constant as a function of resolution for a given ^{12}CO transition, and only slightly varying as a function of ^{12}CO transition at a resolution of 200 pc.

For NGC 4569 the Pearson correlation coefficient is approximately invariant with respect to the resolution, from 74 to 200 pc, for a given ^{12}CO transition. In contrast to this, r_{corr} varies as a function of ^{12}CO line at a given resolution (i.e. 200 pc). The best r_{corr} is obtained with the $^{12}\text{CO}(2-1)$ line ($\sim 0.5-0.6$), while the worst one with the $^{12}\text{CO}(3-2)$ transition (~ 0.3) ($^{12}\text{CO}(1-0)$ gives $r_{\text{corr}} \sim 0.4$).

As in NGC 3627, NGC 4569 has a short molecular τ_{depl} of ~ 1 Gyr, suggesting that the gas is efficiently converted in stars. Within a radius of 0.5 kpc, τ_{depl} is even smaller assuming values of $\sim 0.7-0.9$ Gyr.

4.3. NGC 4579

NGC 4579 (Messier 58) is a SAB(rs)b galaxy classified as an intermediate type 1 object (LINER/Seyfert 1.9) by Ho et al. (1997) at a distance of 20 Mpc in the Virgo cluster. It also has an unresolved nuclear hard X-ray (variable) source with a prominent broad Fe $K\alpha$ line (Terashima et al. 2000; Ho et al. 2001; Eracleous et al. 2002; Dewangan et al. 2004). A non-thermal radio continuum source is detected at the position of the AGN (Hummel et al. 1987; Ho & Ulvestad 2001; Ulvestad & Ho 2001; Krips et al. 2007). The NIR K-band image of NGC 4579 has revealed a large-scale stellar bar and a weak nuclear oval (García-Burillo et al. 2009). The 21 cm H I line observations have shown that the atomic gas in NGC 4579 is currently piling up in a pseudo-ring (radius of $\sim 40''$, ~ 4 kpc) formed by two winding spiral arms that are morphologically decoupled from the bar structure (Haan et al. 2008). Molecular gas in the inner $r \leq 2$ kpc disk is distributed in two spiral arms, an outer arc, and a central lopsided disk-like structure (García-Burillo et al. 2009). The derived gravity torque budget in NGC 4579 have shown that inward gas flow is occurring on different spatial scales in the disk, with a clear *smoking gun* evidence of inward gas transport down to $r \sim 50$ pc.

The panels of the third line of Fig. 1 show that in NGC 4579 Σ_{H_2} and Σ_{SFR} have completely different distributions both at res-

olution of $\sim 1''.6$ (~ 154 pc from $^{12}\text{CO}(1-0)$) and $\sim 0''.8$ (~ 76 pc from $^{12}\text{CO}(2-1)$). Σ_{SFR} is centrally concentrated within the inner $\sim 4''$ (on the plane of the sky) and, at larger distances from the center, lies along two spiral arms extending up to $\sim 12''$ from the nucleus. The morphology of Σ_{H_2} , traced by $^{12}\text{CO}(1-0)$ and $^{12}\text{CO}(2-1)$ is instead mainly defined by two highly contrasted spiral lanes without a central peak (García-Burillo et al. 2009).

Figure 4 shows the results obtained from the analysis of the K-S relation for NGC 4579. N_{fit} ranges from ~ 0.5 to ~ 1.1 at spatial scales of 76–200 pc and taking into account $^{12}\text{CO}(1-0)$ and $^{12}\text{CO}(2-1)$ lines for Σ_{H_2} derivation. For a given ^{12}CO line, N_{fit} decreases with finer resolution. While for $^{12}\text{CO}(1-0)$ N_{fit} gradually decreases from ~ 0.9 at 200 pc-resolution to ~ 0.8 at 154 pc-resolution, for $^{12}\text{CO}(2-1)$ the decreasing of N_{fit} is stronger, from 1.1 to 0.5, possibly because the change from 200 to 76 pc in resolution is more drastic. At the common resolution of 200 pc N_{fit} increases with higher J -CO transition.

In NGC 4579, the quality of the correlation tends to worsen with resolution. While for $^{12}\text{CO}(1-0)$ r_{corr} is approximately constant (~ 0.6) through 154–200 pc resolution, for $^{12}\text{CO}(2-1)$ it drops down from 0.6 to 0.5 in the resolution range from 200 to 76 pc. The correlation coefficient r_{corr} does not seem to depend on the CO transition since it is ~ 0.6 for both ^{12}CO lines at the common resolution of 200 pc.

Unlike NGC 3627 and NGC 4569, NGC 4579 has a more “standard” molecular τ_{depl} of ~ 2 Gyr (see later discussion in Sect. 5.2), without a radial trend.

The similar trends obtained for N_{fit} and r_{corr} as a function of the resolution and for both the two lowest ^{12}CO transitions suggest that in NGC 4579 the K-S relation is almost invariant with respect to $^{12}\text{CO}(1-0)$ and $^{12}\text{CO}(2-1)$ emission lines, but it changes slightly with spatial resolution.

4.4. NGC 4826

NGC 4826, also known as the “Black Eye” or “Evil Eye” galaxy due to its optical appearance, is the closest target (~ 5 Mpc) of the NUGA core sample and its nucleus is classified as a LINER type (Ho et al. 1997). It hosts two nested counter-rotating atomic and molecular gas disks of comparable mass ($\sim 10^8 M_{\odot}$, Braun et al. 1992; Casoli & Gerin 1993; Braun et al. 1994). The inner disk has a radius of $\sim 50''$ (~ 1.3 kpc), while the outer one from $\sim 80''$ to $\sim 9''.8$ ($\sim 2.1 - 15.3$ kpc). Rix et al. (1995), by studying the stellar kinematics along the principal axes of NGC 4826, found that the stars rotate at all radii with the same sense as the inner disk providing strong evidence that stars and gas are coplanar. NUGA observations have shown a large concentration of molecular gas (in $^{12}\text{CO}(1-0)$, $^{12}\text{CO}(2-1)$, and $^{12}\text{CO}(3-2)$), within a radius of 80 pc forming a circumnuclear molecular disk. A detailed analysis of the kinematics, however, does not reveal any evidence of fueling of the nucleus.

The panels of the fourth line of Fig. 1 show the comparison between Σ_{H_2} and Σ_{SFR} distributions in NGC 4826 at resolution of $\sim 2''.1$ (~ 56 pc from $^{12}\text{CO}(1-0)$), $\sim 0''.7$ (~ 17 pc from $^{12}\text{CO}(2-1)$), and $\sim 2''.3$ (~ 59 pc from $^{12}\text{CO}(3-2)$). Unlike NGC 4569 and NGC 4579, the morphologies of Σ_{SFR} and Σ_{H_2} in NGC 4826 are spatially coincident and characterized by a structured disk.

Figure 5 and the right panel of Fig. 6 show the molecular K-S relation derived for NGC 4826 with Σ_{H_2} estimated from the three lowest ^{12}CO emission lines at the intrinsic resolution of the gas maps. As in NGC 3627, there are some cases where only four or five data points are involved in the analysis ($^{12}\text{CO}(2-1)$ and $^{12}\text{CO}(3-2)$ at 200 pc). Neglecting these cases, the K-S relation derived from $^{12}\text{CO}(1-0)$ shows that N_{fit} decreases from ~ 1.3

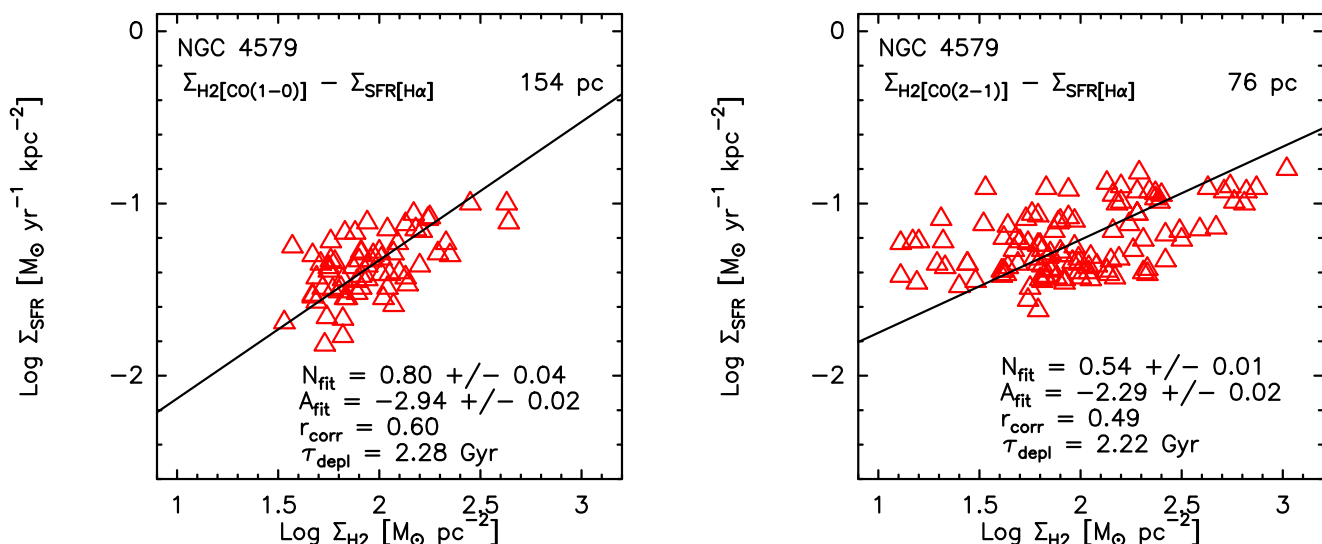


Fig. 4: *Left panel*: Same as left panel of Fig. 2 for NGC 4579 at the resolution of 154 pc. Red triangles indicate data points above 3σ significance both in Σ_{H_2} and Σ_{SFR} , within a radius of 2.7 kpc (on the plane of the galaxy). *Right panel*: Same as left panel with Σ_{H_2} derived from the $^{12}\text{CO}(2-1)$ emission line map at the resolution of 76 pc. Red triangles indicate data points above 3σ significance both in Σ_{H_2} and Σ_{SFR} , within a radius of 1.5 kpc (on the plane of the galaxy).

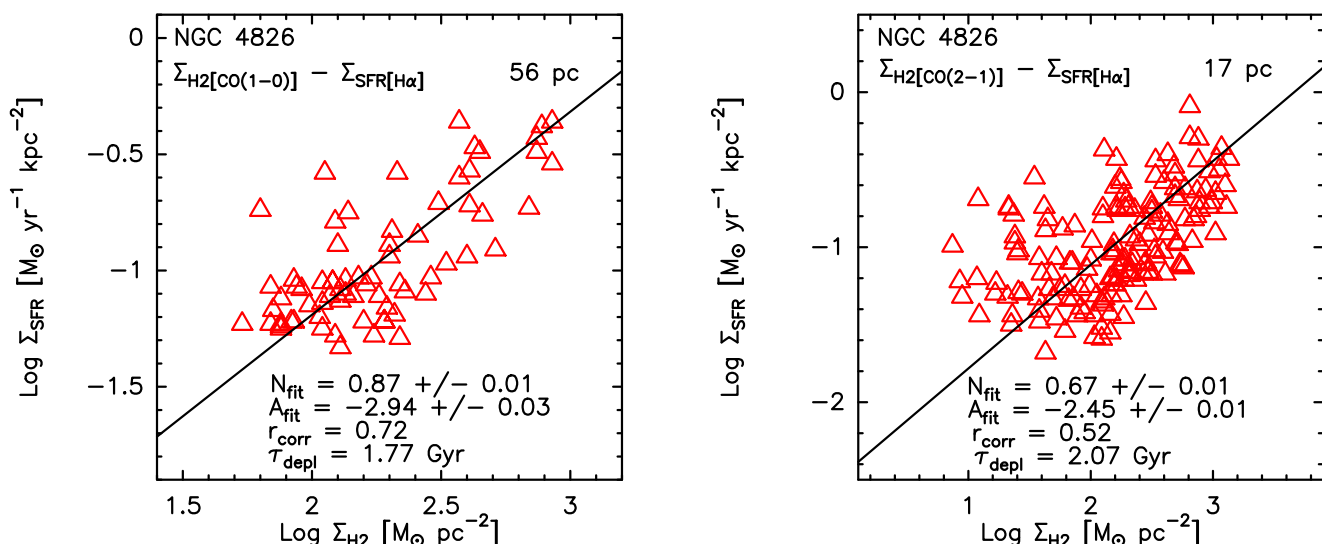


Fig. 5: *Left panel*: Same as left panel of Fig. 2 for NGC 4826 at the resolution of 56 pc. Red triangles indicate data points above 3σ significance both in Σ_{H_2} and Σ_{SFR} , within a radius of 1.1 kpc (on the plane of the galaxy). *Right panel*: Same as left panel with Σ_{H_2} derived from the $^{12}\text{CO}(2-1)$ emission line map at the resolution of 17 pc. Red triangles indicate data points above 3σ significance both in Σ_{H_2} and Σ_{SFR} , within a radius of 0.6 kpc (on the plane of the galaxy).

at 200 pc-resolution to ~ 0.9 at 56 pc-resolution. The case with $^{12}\text{CO}(1-0)$ at 200 pc has a super-linear N_{fit} , while those analyzed at the intrinsic resolution of the all three ^{12}CO maps (17–59 pc) are sub-linear. The comparison between the K-S relation with $^{12}\text{CO}(1-0)$ at 56 pc and that with $^{12}\text{CO}(3-2)$ at 59 pc gives an almost identical N_{fit} (~ 0.9).

The good agreement between Σ_{SFR} and Σ_{H_2} distributions (Fig. 1) consequently corresponds to a high Pearson correlation coefficient, equal to ~ 0.7 – 0.8 for all the cases with more than five data points at resolutions of 56–200 pc. These values of r_{corr} are the best in our sample of galaxies. r_{corr} drops down to ~ 0.5 in the case using the $^{12}\text{CO}(2-1)$ line at 17 pc, the highest resolution available not only in NGC 4826 but also in the present study. This drop of r_{corr} could be due to the high resolution; however, the comparison with the K-S relationship derived using the

$^{12}\text{CO}(2-1)$ line at 200 pc is not definitive proof of this because of the poor number statistics. For other sample galaxies (NGC 4569 and NGC 4579), there is no a strong difference in r_{corr} between $^{12}\text{CO}(1-0)$ and $^{12}\text{CO}(2-1)$. In addition to N_{fit} , also r_{corr} assumes similar values (0.7–0.8) in the cases of $^{12}\text{CO}(1-0)$ at 56 pc and $^{12}\text{CO}(3-2)$ at 59 pc. The results obtained for N_{fit} and r_{corr} suggest therefore that NGC 4826 has a K-S relationship independent of the ^{12}CO transition at resolutions as high as ~ 60 pc.

Like NGC 4579, NGC 4826 has a τ_{depl} of ~ 2 Gyr without radial trend both by using $^{12}\text{CO}(1-0)$ and $^{12}\text{CO}(2-1)$, taking into account only the statistically significant cases. The use of the $^{12}\text{CO}(3-2)$ line instead gives a shorter τ_{depl} , of ~ 1 Gyr, and radial trend since it goes from ~ 1 Gyr within $r < 1.0$ kpc to ~ 0.7 Gyr within $r < 0.2$ kpc.

Table 4: Derived parameters from the pixel-by-pixel molecular star-formation relation for each galaxy.

Galaxy	¹² CO transition	Spatial resolution [pc]	FoV _{sky} [$''$]	r_{gal} [kpc]	$N_{\text{fit(OLS bis.)}}$	$A_{\text{fit(OLS bis.)}}$	$r_{\text{corr(OLS bis.)}}$ (n. pts)	$N_{\text{fit(RR)}}$	$A_{\text{fit(RR)}}$	$\langle \Sigma_{\text{H}_2} \rangle$ [$M_{\odot} \text{pc}^{-2}$]	$\langle \Sigma_{\text{SFR}} \rangle$ [$M_{\odot} \text{yr}^{-1} \text{kpc}^{-2}$]	τ_{depl} [Gyr]	scale [$''/\text{pix}$]
(1)	(2)	(3)	(4)	(5)	(6)	(7)	(8)	(9)	(10)	(11)	(12)	(13)	(14)
NGC 3627	(1-0)	82	24	1.3	1.18 ± 0.11	-3.66 ± 0.19	0.69 (12)	0.83 ± 0.27	-2.72 ± 0.73	50.69	0.04	1.17	2.0
	(1-0)	200	24	1.3	1.11 ± 0.41	-3.47 ± 0.74	0.70 (4)	0.75 ± 0.18	-2.47 ± 0.47	53.60	0.04	1.49	4.0
	(2-1)	36	20	1.1	1.16 ± 0.05	-3.70 ± 0.07	0.62 (88)	0.72 ± 0.10	-2.63 ± 0.27	82.32	0.06	1.27	0.8
	(2-1)	200	20	1.1	1.59 ± 0.63	-4.76 ± 0.92	0.65 (4)	1.06 ± 1.05	-3.32 ± 2.79	75.19	0.05	1.45	4.0
NGC 4569	(1-0)	154	30	3.1	0.60 ± 0.03	-1.96 ± 0.03	0.42 (37)	0.18 ± 0.08	-1.02 ± 0.19	51.40	0.16	1.03	2.0
	(1-0)	200	30	3.1	0.61 ± 0.05	-2.02 ± 0.06	0.43 (30)	0.24 ± 0.10	-1.21 ± 0.22	50.43	0.21	0.99	2.5
	(2-1)	74	20	2.1	0.59 ± 0.01	-1.99 ± 0.01	0.59 (145)	0.32 ± 0.04	-1.37 ± 0.09	116.29	0.36	1.17	1.0
	(2-1)	200	20	2.1	0.64 ± 0.05	-2.11 ± 0.11	0.54 (20)	0.35 ± 0.13	-1.45 ± 0.30	92.68	0.31	1.12	2.5
	(3-2)	190	30	2.9	0.67 ± 0.04	-2.23 ± 0.11	0.27 (39)	0.07 ± 0.06	-0.96 ± 0.14	46.50	0.27	1.05	2.5
	(3-2)	200	30	2.9	0.69 ± 0.08	-2.28 ± 0.08	0.30 (36)	0.08 ± 0.07	-0.99 ± 0.16	42.63	0.25	1.03	2.5
NGC 4579	(1-0)	154	36	2.7	0.80 ± 0.04	-2.94 ± 0.02	0.60 (65)	0.47 ± 0.08	-2.27 ± 0.16	17.36	0.01	2.28	1.8
	(1-0)	200	36	2.7	0.91 ± 0.01	-3.13 ± 0.02	0.58 (61)	0.57 ± 0.09	-2.48 ± 0.18	17.05	0.01	2.07	2.0
	(2-1)	76	20	1.5	0.54 ± 0.01	-2.29 ± 0.02	0.49 (111)	0.24 ± 0.04	-1.69 ± 0.08	40.64	0.02	2.22	1.0
	(2-1)	200	20	1.5	1.14 ± 0.03	-3.49 ± 0.03	0.62 (40)	0.71 ± 0.16	-2.66 ± 0.31	37.76	0.02	1.60	2.0
NGC 4826	(1-0)	56	40	1.1	0.87 ± 0.03	-2.94 ± 0.03	0.72 (70)	0.64 ± 0.07	-2.43 ± 0.17	41.38	0.02	1.77	2.0
	(1-0)	200	40 ^(a)	1.1	1.27 ± 0.08	-3.89 ± 0.05	0.77 (12)	0.91 ± 0.25	-3.09 ± 0.53	105.07	0.05	1.98	7.6
	(2-1)	17	20	0.6	0.67 ± 0.01	-2.45 ± 0.01	0.52 (158)	0.33 ± 0.04	-1.71 ± 0.10	112.31	0.05	2.07	1.0
	(2-1)	200	20 ^(b)	0.6	1.64 ± 1.31	-4.17 ± 0.86	0.49 (4)	0.90 ± 1.13	-2.71 ± 2.26	99.85	0.13	0.79	7.6
	(3-2)	59	36	1.0	0.89 ± 0.04	-2.73 ± 0.07	0.76 (27)	0.64 ± 0.11	-2.19 ± 0.24	16.28	0.02	1.07	2.0
	(3-2)	200	36 ^(c)	1.0	1.22 ± 0.11	-3.19 ± 0.17	0.91 (5)	1.11 ± 0.30	-3.00 ± 0.53	20.93	0.03	0.61	7.6

Notes. ^(a) The effective FoV is reduced to $30''4$ since we rebinned $40''$ with a pixel scale of $7''6$. ^(b) The effective FoV is reduced to $15''2$ since we rebinned $20''$ with a pixel scale of $7''6$. ^(c) The effective FoV is reduced to $30''4$ since we rebinned $36''$ with a pixel scale of $7''6$.

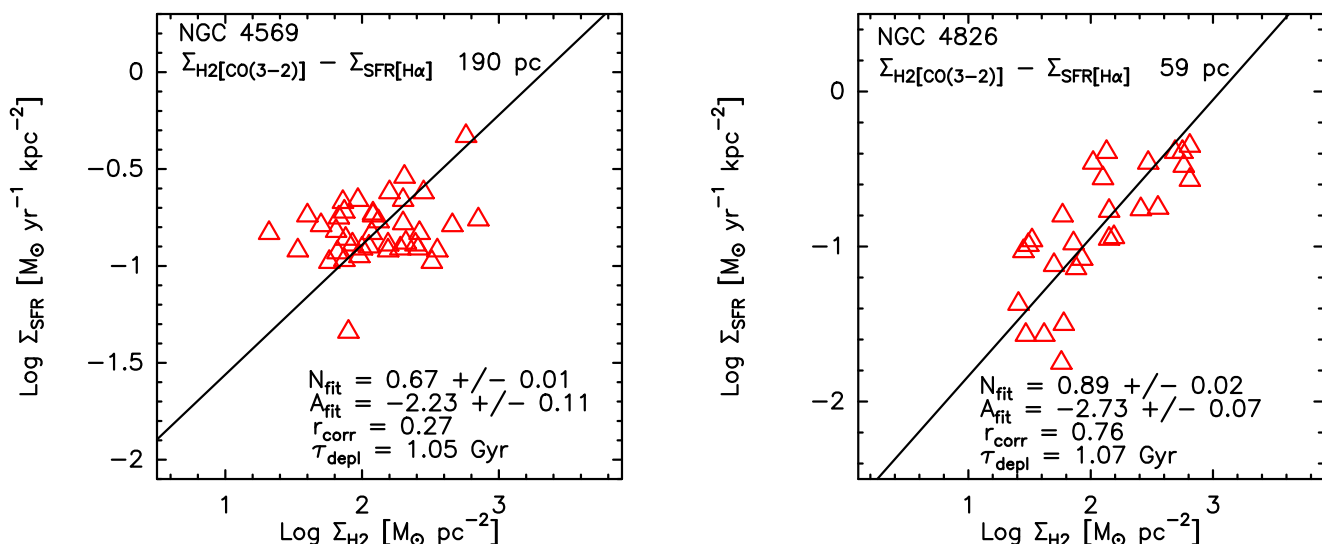


Fig. 6: *Left panel*: Same as Fig. 3, for NGC 4569, with Σ_{H_2} derived from the $^{12}\text{CO}(3-2)$ emission line map based on equation (4) at the resolution of 190 pc. Red triangles indicate data points above 3σ significance both in Σ_{H_2} and Σ_{SFR} , within a radius of 2.9 kpc (on the plane of the galaxy). *Right panel*: Same as left panel for NGC 4826 at the resolution of 59 pc. Red triangles indicate data points above 3σ significance both in Σ_{H_2} and Σ_{SFR} , within a radius of 1.0 kpc (on the plane of the galaxy).

Table 5: Derived parameters from the pixel-by-pixel molecular star-formation relation across the sample at the common spatial resolution of 200 pc.

^{12}CO transition (1)	N_{fit} (2)	A_{fit} (3)	r_{corr} (n.pts) (4)
(1-0)	1.20 ± 0.03	-3.60 ± 0.01	0.66 (107)
(2-1)	1.14 ± 0.01	-3.41 ± 0.02	0.77 (68)
(3-2)	0.67 ± 0.02	-2.22 ± 0.08	0.41 (41)
(1-0)+(2-1)+(3-2)	1.14 ± 0.01	-3.41 ± 0.01	0.64 (216)

5. The molecular star-formation relation across the sample

The analysis performed for each galaxy showed a wide range of behaviors in terms of the K-S relations and that there is no an “universal” molecular SF relation although the investigated galaxies belong to the same sub-class of objects (i. e. nearby active galaxies) and all the derived quantities have been treated with the same methodology and at comparable spatial resolutions. The main result is therefore that each galaxy has its own SF relation (with its own index N_{fit} , correlation coefficient, and τ_{depl}) at spatial scales of ~ 20 –200 pc. Nevertheless, we identified some common behaviors in terms of K-S relation, discussed below.

5.1. The K-S relation index: resolution vs. ^{12}CO transitions

By using the three lowest ^{12}CO at resolutions of ~ 20 –200 pc, we found K-S relation indexes N_{fit} ranging from ~ 0.5 to ~ 1.6 , all values consistent with literature results. A super-linear slope of the K-S relation is consistent both with the early global studies on the SF relation by Kennicutt (1998a) and Kennicutt (1998b) based on the combination of atomic and molecular gas data for the Σ_{gas} computation and with more recent works based only on molecular component at sub-kpc scales (e.g., Kennicutt et al.

2007; Verley et al. 2010; Liu et al. 2011; Rahman et al. 2011; Momose et al. 2013). Bigiel et al. (2008) instead derived $N \sim 1$ from the correlation between Σ_{SFR} and Σ_{H_2} estimated from $^{12}\text{CO}(2-1)$ data for seven nearby spiral galaxies. As already mentioned in Sect. 1, Bigiel et al. (2008) suggested that a linear correlation is evident in regions of high gas surface densities where the gas is typically molecular ($\geq 10 \text{ M}_\odot \text{ pc}^{-2}$). Other studies using $^{12}\text{CO}(2-1)$ also showed a linear correlation (e.g., Leroy et al. 2008; Schruba et al. 2011), including one which combined single-dish $^{12}\text{CO}(2-1)$ data with interferometric $^{12}\text{CO}(1-0)$ data (Rahman et al. 2011). These $^{12}\text{CO}(2-1)$ studies analyzed a substantial number of nearby galaxies, though it should be recognized that some studies based on $^{12}\text{CO}(1-0)$ data showed a super-linear (power-law) correlation, rather than a linear correlation (e.g., Wong & Blitz 2002; Kennicutt et al. 2007; Liu et al. 2011). This suggests that the choice of the CO transition for deriving Σ_{H_2} could affect N_{fit} values (see Bigiel et al. 2008). A linear slope has been also found by Vutisalchavakul et al. (2014) for the SF relation in an 11 deg^2 region of the Galactic plane with dust continua at 1.1 mm and $22 \mu\text{m}$ emission used as tracers of molecular gas and SFR, respectively, over a range of resolution from $33''$ to $20'$ (~ 0.1 –45 pc).

The most common explanation for a linear K-S relationship is that the observed CO luminosity is directly proportional to the number of star-forming clouds or GMCs, with all clouds having similar properties, such as the volume density, the efficiency of the cloud, and the SFR. In observations at resolution ≥ 100 pc, the individual clouds are not resolved but rather their CO flux is dispersed throughout the beam. In this case, regions with more clouds emit more CO in proportion to the number of clouds. Other recent works favor a sub-linear ($N \sim 0.6 - 0.8$) K-S relationship at resolutions ≥ 170 pc (e.g., Blanc et al. 2009; Ford et al. 2013; Shetty et al. 2013, 2014). A sub-linear K-S relationship, in contrast with a linear one, suggests that the clouds do not have the same properties, and SFRs and/or volume densities vary (Shetty et al. 2014). This means that there is no one-to-one correspondence between the CO luminosity and the number of clouds. In addition, the conversion factor X_{CO} also varies

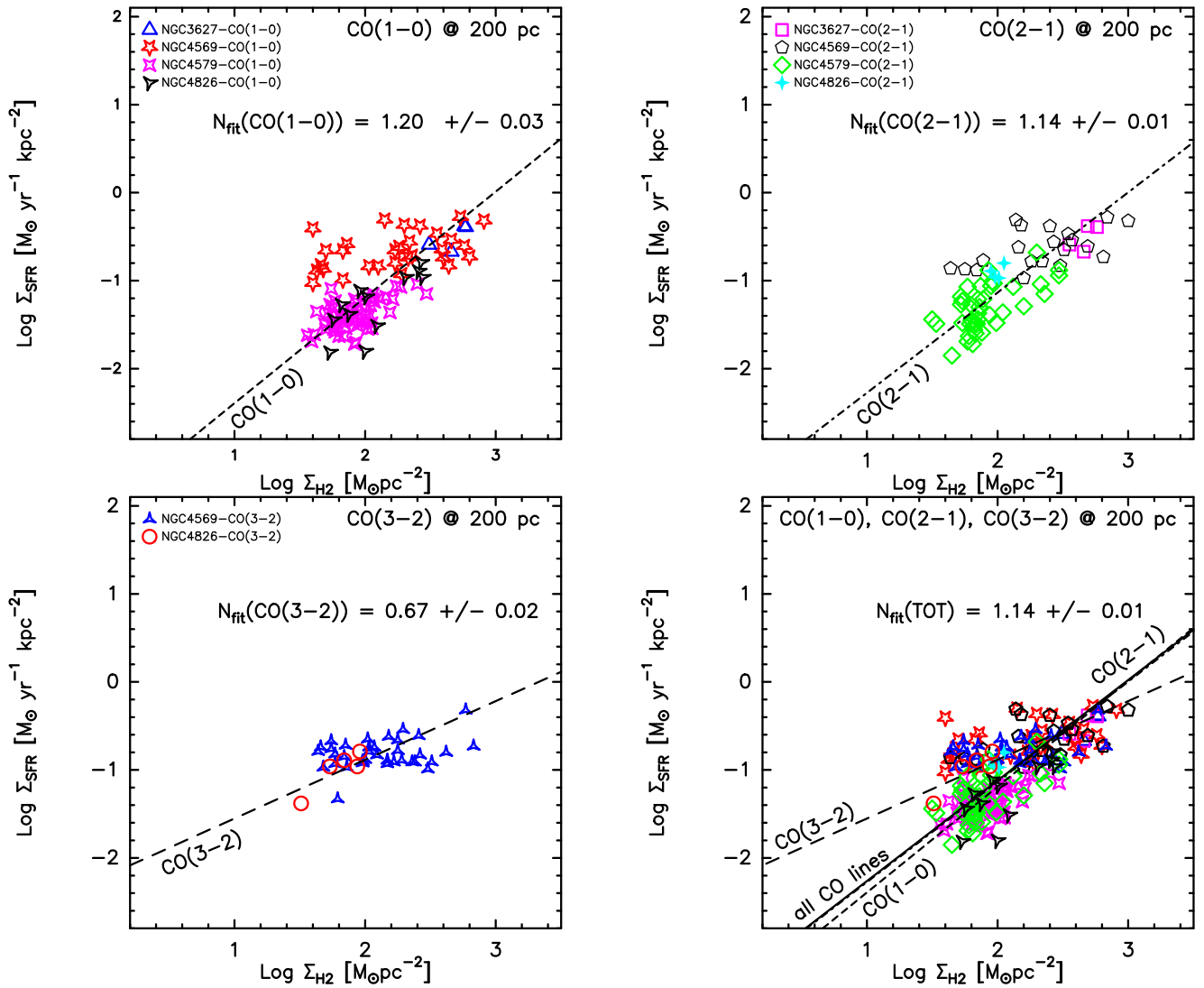


Fig. 7: The K-S relation plot for all sample galaxies. The top left panel plots all galaxies and only $^{12}\text{CO}(1-0)$ emission line data, the top right panel all galaxies and only $^{12}\text{CO}(2-1)$ emission line data, the bottom left panel all galaxies and only $^{12}\text{CO}(3-2)$ emission line data, and the bottom right panel all galaxies and all the available ^{12}CO emission line data, at the common spatial resolution of 200 pc. Different symbols and/or colors indicate galaxies whose Σ_{H_2} has been derived from a given ^{12}CO transition, as shown in the labels. The black lines refer to the OLS fits derived for different cases: the short-dotted line is for all galaxies and $^{12}\text{CO}(1-0)$ emission line data, the point-dotted line for all galaxies and $^{12}\text{CO}(2-1)$, the long-dotted line for all galaxies and $^{12}\text{CO}(3-2)$, and the black solid line is for all galaxies and all the available ^{12}CO lines. In the bottom right panel the $^{12}\text{CO}(2-1)$ OLS fit line is hidden by total OLS fit line.

with the location in a galaxy (see later Sect. 6.1). Finally, a more straightforward explanation for the sub-linear K-S relationship would be that CO permeates the hierarchical interstellar medium, including the filaments and lower density regions within which GMCs are embedded (Shetty et al. 2013, 2014).

From Table 4 it emerges that for a given ^{12}CO transition, the index N_{fit} tends to gradually decrease with finer resolution down to a resolution of approximately 20 pc. On the other hand, on scales larger than ~ 100 pc the slope of the SF relation tends to increase and become somewhat super-linear. This result is common to all the three lowest ^{12}CO transitions and to all galaxies except for NGC 4569 whose N_{fit} is almost constant as a function of resolution as shown in the previous section. Our study suggests therefore that ~ 80 – 100 pc is the scale at which the K-S relation undergoes a change, both with respect to kpc scales and slightly finer spatial scales ($\lesssim 250$ pc, e.g., Bigiel et al. 2008, and

this work). This contrasts with previous results by Onodera et al. (2010) for the Local Group spiral galaxy M 33, in which the slope steepens and the correlation virtually disappears on small spatial scales of ~ 80 pc (i.e. GMC scales). However, in M 33, both the SFR and gas surface densities at 80 pc resolution are significantly lower than in the NUGA sample.

For distinguishing effects on the K-S relation index of different ^{12}CO transitions to derive Σ_{H_2} , data are needed at a common resolution, 200 pc in the present work. The results from this comparison are displayed and collected in Fig. 7 and Table 5, respectively. Each panel of Fig. 7 shows the K-S relation plot for all sample galaxies and both taking into account separately the three ^{12}CO lines and all together without distinction based on the transition. Different symbols and/or colors indicate galaxies whose Σ_{H_2} has been derived from a given ^{12}CO transition and the black lines refer to the OLS fits derived for different cases. At the

resolution of 200 pc, taking into account all sample galaxies and separately $^{12}\text{CO}(1-0)$ (top left panel) and $^{12}\text{CO}(2-1)$ (top right panel), the resulting K-S relations have indices of 1.20 ± 0.03 and 1.14 ± 0.01 , respectively. These findings indicate that $^{12}\text{CO}(1-0)$ and $^{12}\text{CO}(2-1)$ lines lead to quite similar results in terms of the slope of the K-S relation. Under the same conditions but by using $^{12}\text{CO}(3-2)$ data (bottom left panel) we found a sub-linear slope of 0.67 ± 0.02 . However, this result is based only on two cases, NGC 4569 and NGC 4826, and for NGC 4569 all slopes for the three lowest ^{12}CO transitions at all investigated resolutions (74–200 pc) are sub-linear. Vice versa, in NGC 4826 the slope derived from the $^{12}\text{CO}(3-2)$ line is roughly unity at 200 pc of resolution (see Table 4). Taking into account all sample galaxies and all available ^{12}CO transitions (bottom left panel), the K-S relation has a “standard” index of 1.14 ± 0.01 .

It is well known that each transition traces different physical gas properties. The kinematic temperature of molecular gas is typically of ~ 10 K (Scoville et al. 1987), which above the level energy temperature of 5.5 K for the $J = 1$ level of the ^{12}CO , but below the temperatures of 16.5 K and 33 K for the $J = 2$ and $J = 3$ levels, respectively. This implies that a slight change in gas kinematic temperature is sufficient to affect the excitation for the $^{12}\text{CO}(2-1)$ and $^{12}\text{CO}(3-2)$ emission lines. The different critical densities of the three ^{12}CO transitions ($\sim 10^3 \text{ cm}^{-3}$, $\sim 2 \times 10^4 \text{ cm}^{-3}$, and $\sim 7 \times 10^4 \text{ cm}^{-3}$ for $^{12}\text{CO}(1-0)$, $^{12}\text{CO}(2-1)$, and $^{12}\text{CO}(3-2)$, respectively) make their line ratios sensitive to local gas density. R_{21} has been observed to systematically vary with SFR and Σ_{gas} in the Milky Way (e.g., Sakamoto et al. 1995; Sawada et al. 2001) and M 51 (Koda et al. 2012; Vlahakis et al. 2013). Despite this, because of the use of individually measured mean R_{32} to convert to an equivalent CO(1–0) mass conversion, such variations do not have a significant impact on the resulting index N_{fit} of the K-S relation.

Another result emerging from Table 4 concerns the K-S relation studied at 200 pc resolution with Σ_{H_2} derived from $^{12}\text{CO}(1-0)$. NGC 3627, NGC 4579, and NGC 4826 exhibit K-S relations with indices N_{fit} around unity, with Σ_{H_2} of ~ 20 – $100 M_{\odot} \text{ pc}^{-2}$, and τ_{depl} of ~ 1.5 – 2 Gyr. NGC 4569 is different from the other sample galaxies also in this respect; it has indeed a Σ_{H_2} of $\sim 50 M_{\odot} \text{ pc}^{-2}$, comparable to the other galaxies, but its K-S relation has a sub-linear slope and τ_{depl} of ~ 1 Gyr.

5.2. The molecular gas depletion time

As discussed in Sect. 1, τ_{depl} is an important parameter in the study of the K-S relation together with the power index N_{fit} for understanding the SF phenomenon in galaxies. We found molecular τ_{depl} ranging from ~ 1 to ~ 2 Gyr, consistent with the more recent literature results as discussed below. Each galaxy has its own τ_{depl} that seems to be invariant with respect to the spatial scale probed in a given galaxy, at resolutions from ~ 20 to 200 pc. The molecular τ_{depl} is also invariant with respect to $^{12}\text{CO}(1-0)$ and $^{12}\text{CO}(2-1)$ lines. The discussion on the τ_{depl} derived from $^{12}\text{CO}(3-2)$, for NGC 4569 and NGC 4826, deserves a separate treatment and will be discussed later.

Both NGC 3627 and NGC 4569 have molecular τ_{depl} of ~ 1 – 1.3 Gyr, by using $^{12}\text{CO}(1-0)$ and $^{12}\text{CO}(2-1)$ and taking into account only the statistically significant cases. These values of τ_{depl} are compatible with the mean molecular [$^{12}\text{CO}(1-0)$] τ_{depl} of ~ 1.2 Gyr (with $\alpha_{\text{CO}} = 3.5 M_{\odot} (\text{K km s}^{-1} \text{ pc}^{-2})^{-1}$) found by Saintonge et al. (2011) for the COLD GASS sample of more than 200 galaxies at distances of ~ 100 – 200 Mpc, but lower than the mean molecular [$^{12}\text{CO}(2-1)$] τ_{depl} of ~ 2 Gyr found by

Bigiel et al. (2008) and Leroy et al. (2008) in the HERACLES survey consisting of a sample of 48 nearby ($D \sim 3$ – 20 Mpc) galaxies. NGC 3627 and NGC 4569 have therefore a τ_{depl} more consistent with the COLD GASS single-dish survey that gives a global picture of gas and SF in the Local Universe but lacks the power to trace the exact distribution of these components, rather than with the HERACLES survey that, like the present study, maps them. However, Saintonge et al. (2011) demonstrated that after using the same conversion factor from CO luminosity and H_2 mass ($\alpha_{\text{CO}} = 3.5 M_{\odot} (\text{K km s}^{-1} \text{ pc}^{-2})^{-1}$) and restricting the HERACLES sample to the COLD GASS stellar mass range, the mean molecular τ_{depl} for HERACLES is ~ 1 Gyr, consistent with the COLD GASS estimate.

As mentioned in Sect. 4.2, τ_{depl} of NGC 4569 also shows a hint of radial trend reaching values of ~ 0.7 – 0.9 Gyr within a radius of 0.5 kpc. These low values for the molecular τ_{depl} are in line also with the recent results by Faesi et al. (2014) for NGC 300 at 250 pc scales, slightly larger although comparable to ours, and by Lada et al. (2010) for the Milky Way GMCs, who found depletion times of ~ 0.2 Gyr. Since Faesi et al. (2014) studied the relation between molecular gas and SF in 76 HII regions of NGC 300, they concluded that the short τ_{depl} arises because their analysis accounts for only the gas and stars within the youngest star-forming regions. These depletion times correspond to the timescale for SF to consume the gas reservoir in the star clusters’ parent GMCs, which may be the more relevant quantity in the context of GMC-regulated SF in galaxies. The hint of radial trend of τ_{depl} in NGC 4569 also suggests that SF becomes more inefficient at larger radii under the assumption of a fixed X_{CO} conversion factor. This finding is in agreement with results obtained by Leroy et al. (2013) who found systematically lower τ_{depl} for a given X_{CO} in the inner kpc of a sample of 30 galaxies, among AGN and starbursts. Since X_{CO} is typically smaller closer to galaxy nuclei (Sandstrom et al. 2013) implying shorter τ_{depl} for a given CO luminosity, the radial trend of τ_{depl} could be even steeper. The shortening of τ_{depl} toward the very center of NGC 4569 coincides both with a better correlation between Σ_{H_2} and Σ_{SFR} distributions (see Fig. 1) and with an increase in the R_{21} ratio there, indicative of more excited gas. R_{21} ranges from 0.2 to 0.9 in the inner region of NGC 4569 (Boone et al. 2007, 2011), with a smooth and quite symmetric distribution with respect to the center, and continuously increasing toward the nucleus. Similar radial trends in R_{21} , also present in other NUGA galaxies (NGC 4579, NGC 6574: García-Burillo et al. 2009; Lindt-Krieg et al. 2008, respectively) and in the sample of Leroy et al. (2013), presumably reflect similar changing physical conditions that drive the lower X_{CO} factors found by Sandstrom et al. (2013). This would underscore that molecular gas in the central regions gives off more CO emission, appears more excited, and forms stars more rapidly than molecular gas further out in the disks of galaxies. Compared to R_{21} , R_{32} shows a more clumpy and asymmetric distribution within the central region (Boone et al. 2011), differently from the large-scale gradient in R_{32} reported by Wilson et al. (2009). R_{32} is usually expected to probe more extreme physical conditions such as those occurring in star forming or shock regions. Boone et al. (2011) indeed confirmed that R_{32} tracks massive SF in NGC 4569 better than R_{21} by comparing R_{21} and R_{32} maps to the Pa α image as detected by NICMOS (see also Wilson et al. 2009). In any case, in NGC 4569 ^{12}CO is less excited ($R_{32} \sim 0.6$) than in the Galactic Center and most of the centers of normal, starburst, and active galaxies studied so far for which $R_{32} \sim 0.2$ – 5 (e.g., Devereux et al. 1994; Mauersberger et al. 1999; Matsushita et al. 2004; Mao et al. 2010; Combes et al. 2013;

Table 6: Stellar and star formation properties of our galaxy sample.

Galaxy	$\log(M_*)^{(a)}$ [M_\odot]	$\log(\text{TIR})^{(b)}$ [erg s^{-1}]	SFR $^{(c)}$ [$M_\odot \text{ yr}^{-1}$]	$\log(\text{sSFR})$ [yr^{-1}]
(1)	(2)	(3)	(4)	(5)
NGC 3627	10.57 ± 0.13	10.4	4.33	-9.93
NGC 4569	10.38 ± 0.12	9.7	0.86	-10.44
NGC 4579	9.96 ± 0.23	10.1	2.17	-9.62
NGC 4826	9.99 ± 0.12	9.6	0.69	-9.30

Notes. ^(a) Values from Skibba et al. (2011). ^(b) Values from Dale et al. (2012). ^(c) SFR derived adopting calibration from Kennicutt (1998a) for TIR luminosity.

García-Burillo et al. 2014). Shorter τ_{depl} could be also due to the high pressure driven by the deep potential well in the central parts of galaxies, driving gas to higher densities. This effect has been seen both in our Galaxy (Oka et al. 2001) and in others (Rosolowsky & Blitz 2005), and has been suggested to explain shorter τ_{depl} (i.e., enhanced SFE in galaxy centers) in the sample of Leroy et al. (2013).

NGC 4579 and NGC 4826 have instead higher molecular τ_{depl} of ~ 2 Gyr, both with $^{12}\text{CO}(1-0)$ and $^{12}\text{CO}(2-1)$ and taking into account only the statistically significant cases. For NGC 4579, neglecting the case of the net sub-linear K-S relationship found with $^{12}\text{CO}(2-1)$ at the resolution of 76 pc, $\tau_{\text{depl}} \sim 2$ Gyr is accompanied by an index N_{fit} around unity. As already mentioned above, the interpretation of a linear K-S relationship is that CO is primarily tracing star-forming clouds with relatively uniform properties, including Σ_{SFR} , and consequently the τ_{depl} of the CO traced gas is constant and of ~ 2 Gyr, both within and between galaxies. However, there is yet no consensus on either the precise K-S parameter estimates, or the associated interpretation (see Dobbs & Pringle 2013, for a review of explanations of the K-S relationship). In contrast to NGC 4569, τ_{depl} in NGC 4579 does not show a radial trend although R_{21} varies as a function of the radius. Close to the AGN, at $r < 200$ pc, $R_{21} \sim 0.8-1$, whereas at $r > 500$ pc $R_{21} \sim 0.4-0.6$ (García-Burillo et al. 2009).

The use of the $^{12}\text{CO}(3-2)$ line gives a τ_{depl} of ~ 1 Gyr both for NGC 4569 and NGC 4826, suggesting that the gas traced by this transition could be more efficiently converted into stars with respect to $^{12}\text{CO}(1-0)$ and $^{12}\text{CO}(2-1)$ emissions, despite the use of mean $\text{CO}(1-0)/\text{CO}(3-2)$ ratios to convert mass densities. While NGC 4569 has $\tau_{\text{depl}} \sim 1$ Gyr for all the three ^{12}CO lines and for all resolutions taken into account, NGC 4826 shows a lower $^{12}\text{CO}(3-2)$ τ_{depl} than those derived from $^{12}\text{CO}(1-0)$ and $^{12}\text{CO}(2-1)$ (~ 2 Gyr). In addition, for NGC 4826 while τ_{depl} does not show a radial trend in the cases of $^{12}\text{CO}(1-0)$ and $^{12}\text{CO}(2-1)$, this trend is seen by using $^{12}\text{CO}(3-2)$. However, the $^{12}\text{CO}(3-2)$ distribution is similar to that of the $\text{CO}(1-0)$ and $\text{CO}(2-1)$ lines at the same resolution (Boone et al. 2011). In contrast to NGC 4569, in NGC 4826 R_{32} does not appear to be more clumpy than R_{21} , and both maps look relatively symmetric with respect to the dynamical center, with both ratios increasing steadily toward the center (Boone et al. 2011). As in NGC 4569, high R_{32} values (>0.3) occur within the $\text{Pa}\alpha$ emission region as detected by NICMOS, while this is not true for R_{21} that reaches high values (>0.7) away from the $\text{Pa}\alpha$ emitting regions (Boone et al. 2011). This difference, and the variation in R_{32} , could be responsible for the short τ_{depl} inferred by $^{12}\text{CO}(3-2)$ in NGC 4826.

Compared to the $^{12}\text{CO}(1-0)$ and $^{12}\text{CO}(2-1)$, the $^{12}\text{CO}(3-2)$ traces relatively warmer and denser gas. There is also growing evidence that the $^{12}\text{CO}(3-2)$ emission correlates more tightly with the SFR or SFE than does $^{12}\text{CO}(1-0)$ and $^{12}\text{CO}(2-1)$ (e.g., Komugi et al. 2007; Muraoka et al. 2007; Wilson et al. 2009, 2012). Similarly, Iono et al. (2009) showed that the $^{12}\text{CO}(3-2)$ emission correlates nearly linearly with the FIR luminosity for a sample of local luminous IR galaxies and high-redshift submillimeter galaxies. Thus, it appears that the $^{12}\text{CO}(3-2)$ emission is preferentially tracing the molecular gas associated directly with SF, such as high-density gas that is forming stars or warm gas heated by SF, rather than the total molecular gas content of a galaxy usually traced by $^{12}\text{CO}(1-0)$ and $^{12}\text{CO}(2-1)$. Nevertheless, this evidence is not able to explain the shorter τ_{depl} characterizing the $^{12}\text{CO}(3-2)$ -molecular K-S relation for NGC 4826 with respect to $^{12}\text{CO}(1-0)$ and $^{12}\text{CO}(2-1)$. Values of τ_{depl} derived for a given galaxy and within comparable FoVs are indeed expected to be similar for all ^{12}CO lines, by construction, since we are not deriving gas traced by $^{12}\text{CO}(3-2)$ but the total gas assuming a R_{32} line ratio in addition to the X_{CO} conversion factor (see Eq. 4). The bottom right panels of Fig. 7 and Fig. 8 show that Σ_{H_2} data points derived from the $^{12}\text{CO}(3-2)$ line emission have typically lower Σ_{H_2} values with respect to $^{12}\text{CO}(1-0)$ and $^{12}\text{CO}(2-1)$ derivation, but this effect is not due to the choice of the ^{12}CO line but simply to the availability of $^{12}\text{CO}(3-2)$ data only for NGC 4569 and NGC 4826. It is possible that our result is simply due to the variation of R_{32} that could not be taken into account in the mean value used for the derivation of Σ_{H_2} in Eq. 4.

The radial trend of τ_{depl} as a function of physical conditions of gas, typically expressed in terms of line ratios, is not clearly defined. While NGC 4569 exhibits a τ_{depl} decreasing toward the very center together with an increasing of R_{21} , NGC 4579 has a constant τ_{depl} as a function of the radius but a higher R_{21} in the central galaxy region. This difference could be explained by the (dis)agreements between gas and SFR morphologies for the two galaxies. Both NGC 4569 and NGC 4579 are centrally peaked in Σ_{SFR} without a counterpart in Σ_{H_2} (see Fig. 1). However, NGC 4569 shows CO emission in the very center, but NGC 4579 has no gaseous nuclear emission, nor a radial trend in the gas morphology (although the R_{21} line ratio decreases as a function of radius). It appears therefore that the radial trend of τ_{depl} as a function of CO line ratios has to be accompanied also by similar radial trend both in gas and SFR morphologies in a given galaxy.

It is well known that gas depletion times are different in extreme starburst galaxies and merging systems in the local Universe, as well as submillimeter galaxies at high redshifts (e.g. Kennicutt 1998a; Bouché et al. 2007; Riechers et al. 2007; Bothwell et al. 2010). In these galaxies, gas depletion times are

significantly shorter, with the star formation surface density being an order of magnitude larger at fixed gas surface density, compared to the normal galaxy population (Genzel et al. 2010). More recently, it has emerged that the molecular τ_{depl} varies even within the population of nearby ‘normal’ star-forming galaxies and this variation has been quantified as a function of a range of fundamental parameters. Saintonge et al. (2011), Boselli et al. (2014), and Bothwell et al. (2014) found that depletion timescales vary monotonically from ~ 2 Gyr to ~ 0.1 Gyr across 2 orders of magnitude in stellar mass. This finding persists also when using a constant conversion factor and for different conversion factor values (Bothwell et al. 2014). Saintonge et al. (2011) also found that τ_{depl} correlates inversely with the specific SFR (SFR per unit stellar masses, sSFR). Table 6 collects the main stellar and star formation properties of our galaxy sample. In this table, Col. (1) gives the galaxy name, Col. (2) the logarithm of the stellar mass (M_*), Col. (3) the logarithm of the total IR (TIR) luminosity, Col. (4) the SFR derived adopting the conversion of Kennicutt (1998a) for TIR (from 8–1000 μm), and Col. (5) the logarithm of the sSFR. NUGA galaxies have stellar masses in the COLD GAS range ($\log(M_*)$ from 10 to 11.5 M_\odot) and sSFR toward the high end of the COLD GAS sample ($\log(\text{sSFR})$ from -11.8 to -9.5 yr^{-1}), and thus consistent both with our results for short depletion times and the correlation that Saintonge et al. (2011) found between τ_{depl} and sSFR. Nevertheless, the NUGA galaxies with the longest τ_{depl} (although only a factor of 2) have the highest sSFR, although the values are within the scatter found by Saintonge et al. (2011).

The dependence of τ_{depl} on the spatial scale has also been explored by other groups. Schruba et al. (2010) found for M 33 a median $\tau_{\text{depl}} \sim 1.1$ Gyr (using the conversion factor we use here) and with no dependence on type of region targeted at kpc scales, but below these scales τ_{depl} is a strong function of the adopted scale and the type of region that is targeted (see also Komugi et al. 2005, for τ_{depl} even down to 0.1 Gyr in the central few hundred parsecs of local spirals). Schruba et al. (2010) derived very long τ_{depl} (up to 10 Gyr) using small apertures centered on CO peaks, but very short τ_{depl} (0.3 Gyr) with small apertures targeted toward $\text{H}\alpha$ peaks. This may not be surprising, given the disparity of the bright $\text{H}\alpha$ and CO distributions in M 33 (see Fig. 1 in Schruba et al. 2010), similar to the inconsistencies between Σ_{gas} and Σ_{SFR} morphologies characterizing some NUGA galaxies, such as NGC 4569 and NGC 4579 (see Fig 1). Schruba et al. (2010) found that the SF relation in M 33 observed on kpc scales breaks down for aperture sizes of ~ 300 pc. These aperture sizes are larger than the breakdown scale of 80–100 pc found by Onodera et al. (2010) for the same galaxy.

5.3. The dispersion of the data

At the relatively high resolutions τ_{depl} studied here, the Pearson correlation coefficient r_{corr} is generally low and there is large scatter, with values as low as ~ 0.3 .

Angular resolutions of ~ 1 – $2''$ correspond to ~ 20 – 200 pc at the distances of the sample galaxies. An inspection of the maps shown in Fig. 1 reveals that CO intensity peaks are offset from the $\text{H}\alpha$ peak, often by more than ~ 1 – $2''$. In addition, there is the possibility that such small beams do not include both the star-forming region and its counterpart molecular cloud, which is generally several tens of parsecs in size. In general, star-forming regions do not coincide with the molecular clouds that give birth to them. This is typically seen in spiral arms of galaxies, where the optical and molecular spiral structures are offset. If only the molecular clouds are observed, and not the star-forming regions

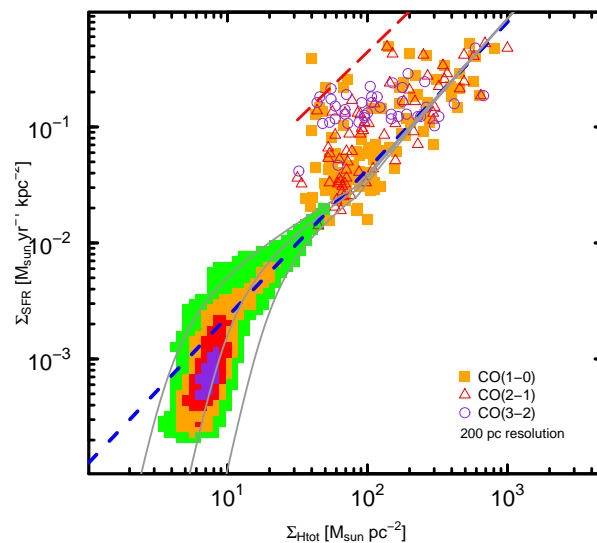


Fig. 8: Comparison between the K-S relation plot derived for all sample galaxies and taking into account all the ^{12}CO emission lines at the common resolution of 200 pc, as shown in Fig. 7, and results from Bigiel et al. (2008). The model predictions from Krumholz et al. (2009) are also shown with solar metallicity and clumping factor $c = 1, 2,$ and 5 ; see Krumholz et al. (2009) for more details. Also shown (as a blue short-dashed line) is the trend for star-forming galaxies and mergers found by Genzel et al. (2010) using a common conversion factor $\alpha_{\text{CO}} (= 3.2 M_\odot \text{pc}^{-2} (\text{K km s}^{-1})^{-1})$. The horizontal axis has been adjusted to our $\alpha_{\text{CO}} (= 3.5 M_\odot \text{pc}^{-2} (\text{K km s}^{-1})^{-1})$ and our non-inclusion of helium. We have also plotted the merger/starburst trend by Genzel et al. (2010) (with $\alpha_{\text{CO}} = 1 M_\odot \text{pc}^{-2} (\text{K km s}^{-1})^{-1}$) as shown by a (red) long-dashed line.

which are physically coupled to them, the gas density would be expected to show an excess over the expected correlation.

For a given galaxy, a given ^{12}CO transition, and taking into account only the statistically significant cases, r_{corr} is quite stable (see NGC 4569) or it tends to decrease with resolution, although this tendency is weak (see NGC 4579 in $^{12}\text{CO}(2-1)$ and NGC 4826 in $^{12}\text{CO}(1-0)$). This latter trend is consistent with the result of a larger scatter at smaller scales found by Vutisalchavakul et al. (2014) studying the SF relation in the Galactic plane. They found that the rank correlation coefficients between $\log(\Sigma_{\text{H}_2})$ and $\log(\Sigma_{\text{SFR}})$ increase from ~ 0.4 to ~ 0.8 in the resolution range from $33''$ to $20'$. Vutisalchavakul et al. (2014) also compared their results with some resolved extragalactic SF relations, available at a scale of about 200 pc (for instance M 33 from Schruba et al. 2010), finding the same trend of the dispersion as a function of resolution for extragalactic data and a smaller scatter in the depletion time distribution for the Galactic plane than for the extragalactic sources.

5.4. The K-S relation at high densities of molecular gas

The range of Σ_{H_2} over which we studied the K-S relation is ~ 20 – $120 M_\odot \text{pc}^{-2}$. These densities are higher than those of 20 – $50 M_\odot \text{pc}^{-2}$ studied by Bigiel et al. (2008) and other authors. The circumnuclear regions examined here are subject to physical conditions different from the disk. Besides

denser gas tracers, such as HCN and HCO⁺, observed in these regions (e.g., Krips et al. 2011; Combes et al. 2013, 2014; García-Burillo et al. 2014), rotation curves in the central kpc are different from disks, following roughly rigid-body rotation compared to nearly flat in the disks (e.g., Sofue et al. 2003). This would lessen the effect of shear, which works on the clouds, and may enhance the efficiency of the SF arising from gravitational collapse. These effects could conspire to produce a systematic change in the K-S relation in the central regions of galaxies. Figure 8 shows the comparison between our results for the whole sample at 200 pc resolution (as also displayed in Fig. 7) and the findings from Bigiel et al. (2008). Also plotted in Fig. 8 are the predictions from the Krumholz et al. (2009) models for solar metallicity and various clumping factors (see Krumholz et al. 2009, for more details). For the comparison we have converted the Σ_{H_2} measurements in Bigiel et al. (2008) to the conversion factor we use here, but have not adjusted the SFRs since the Kroupa IMF (Kroupa 2001) used by them is similar to ours (see Calzetti et al. 2007). Fig. 8 also shows two trends found by Genzel et al. (2010): the (blue) short-dashed line gives the common trend for star-forming galaxies (SFGs) and mergers/starburst using a single conversion factor ($\alpha_{\text{CO}} = 3.2 \text{ M}_{\odot} \text{ pc}^{-2} (\text{K km s}^{-1})^{-1}$); the (red) long-dashed line corresponds to the merger/starburst trend only (with $\alpha_{\text{CO}} = 1 \text{ M}_{\odot} \text{ pc}^{-2} (\text{K km s}^{-1})^{-1}$). Both regressions have been adjusted to our α_{CO} ($3.5 \text{ M}_{\odot} \text{ pc}^{-2} (\text{K km s}^{-1})^{-1}$) and for our non-inclusion of helium.

We find that at densities as high as $\sim 10^3 \text{ M}_{\odot} \text{ pc}^{-2}$ there is reasonable agreement with the predictions of Krumholz et al. (2009). However, with a common conversion factor, the central regions of the NUGA galaxies have higher Σ_{SFR} for a given gas column than would be expected from the models. They fill in the region between the mergers/high- z starburst systems and the more quiescent SFGs studied by Genzel et al. (2010), assuming that the former require a lower value of α_{CO} . The apparently high Σ_{H_2} would also be consistent with the results of Sandstrom et al. (2013) who find that α_{CO} in centers of galaxies relative to their disks can be as much as 10 times lower. We could thus be slightly overestimating Σ_{H_2} in our sample, although exactly by how much is difficult to determine. To assuage the offset between mergers/starbursts and SFGs, Krumholz et al. (2012) have devised a “universal SF law” which is based on volumetric densities (see also Genzel et al. 2010). They argue that such a formulation is particularly important for resolutions of 10–100 pc, similar to that achieved by our observations. In addition, the galaxies studied here are roughly consistent with model predictions of Krumholz & McKee (2005) and Krumholz et al. (2009).

It is difficult to consider the K-S relation for normal galaxies at even higher densities. This would require that we observe with even better spatial resolution (possible with ALMA), but the GMCs would then be highly resolved. Thus we may not be able to observe the molecular cloud and its counterpart star-forming region within one beam, for galaxies –such as those studied here– at distances of ~ 5 –20 Mpc (see Sect. 5.3). It is possible that the K-S relation is fundamentally a correlation seen only when the ISM is averaged over a considerable area. As already discussed in Sect. 5.1, our work shows that the K-S relation undergoes a change at spatial resolution of ~ 80 –100 pc (\sim GMC scale), i.e. its slope starts to sharply decrease with respect to higher scales. The breakdown of the K-S relation could therefore occur at ~ 80 –100 pc, as found by Onodera et al. (2010) for M 33, even if in NUGA dense nuclei a net breakdown is still not visible at scales as high as ~ 20 pc.

6. Caveats

Here we examine possible caveats or systematic uncertainties associated with our analysis and results presented in the previous sections. These can arise from physical reasons connected to our simplified assumptions, from the methodology we used to derive the various quantities, and/or from the adopted fitting method of data.

6.1. Derivation of Σ_{H_2}

It is well known that the X_{CO} conversion factor is a source of systematic uncertainty in the estimate of Σ_{H_2} . By adopting a constant value for X_{CO} , we do not account for its changes with galaxy properties such as physical gas conditions and metallicity (e.g., Maloney & Black 1988; Bolatto et al. 2008; Glover & Mac Low 2011; Magrini et al. 2011; Bolatto et al. 2013). Estimates of “typical” values of X_{CO} in the Milky Way and other spiral galaxies range from $\sim 1.5 \times 10^{20} \text{ cm}^{-2} (\text{K km s}^{-1})^{-1}$ to $\sim 4 \times 10^{20} \text{ cm}^{-2} (\text{K km s}^{-1})^{-1}$.

CO line ratios are typically used to constrain the excitation conditions (temperature, density, and column density) of the line-emitting gas. Some studies have shown that these line ratios (mainly R_{21}) tend to radially vary, with larger values toward galaxy nuclei (e.g., Lindt-Krieg et al. 2008; García-Burillo et al. 2009), and this effect presumably reflects similar changing of physical conditions that drive the lower X_{CO} factors found by Sandstrom et al. (2013). Bolatto et al. (2013), presenting a review of the theoretical underpinning, techniques, and results of efforts to estimate X_{CO} conversion factor in different environments, also stressed that X_{CO} appears to drop in the central, bright regions of some but not all galaxies. The AGN may also play a role since a higher R_{21} toward the center of active galaxies could be interpreted as evidence of external heating of molecular clouds by X-rays in the vicinity of the AGN (e.g., Baker et al. 2003). However, this radial trend of the gas physical conditions does not univocally characterize all the LLAGN of our sample. Although R_{21} ratios show a radial trend, or hints of it, in NGC 4569, NGC 4579, and NGC 4826, R_{21} in NGC 3627 and R_{32} in NGC 4569 and NGC 4579 do not exhibit the same behavior assuming constant or stochastic variation as a function of radius. For the lack of a common trend in our sample we adopted constant values of R_{21} and R_{32} . This assumption may introduce an uncertainty in Σ_{H_2} derivation, although NUGA galaxies benefit from individual measures of line ratios for each galaxy nuclear region, and not a typical value for this class of objects.

As for metallicity, Boissier et al. (2003) and Narayanan et al. (2012) found that by using metallicity dependent X_{CO} , Σ_{H_2} should typically change by a factor of 2 to 3 in the central regions compared to disk regions of nearby spirals, in the sense of decreasing gas mass. Our sample galaxies have all been observed by Moustakas et al. (2010) who find roughly solar metallicities for all, but were unable to evaluate metallicity gradients for lack of data. Nevertheless, because of the relatively small field-of-view afforded by our CO observations, any metallicity gradient is expected to be very slight over the radial range sampled by our data. We therefore adopted a constant X_{CO} for the sake of uniformity and simplicity, as suggested in the review of Bolatto et al. (2013) in absence of a detailed characterization of X_{CO} in a given galaxy and as typically done in the major part of studies aimed at determining molecular gas mass from ¹²CO line intensities.

As already discussed in Sect. 1, we only used molecular (hydrogen) gas in our study based on the assumption that SF formation occurs in molecular cloud cores where H₂ dominates.

This implies a two-step process of SF where H_2 clouds are first formed from H_I , and stars are then formed from H_2 . This leads to the hypothesis that H_2 should be more directly connected with SFR. Moreover, we are interested in galactic centers which are high-density regions of galaxies and can be H_I deficient (e.g., Bigiel et al. 2008). Haan et al. (2008) observed the atomic gas for the galaxies in our sample, but the H_I beam subtends approximately our entire CO FoV, ranging from $\sim 20''$ to $\sim 40''$. With this beam, NGC 4579 has an H_I central hole with a surrounding ring; this galaxy also has the lowest (Σ_{H_2}) in our sample (see Table 4). For the other galaxies, H_I column densities $\Sigma_{HI} \sim 10$ – $13 M_\odot pc^{-2}$ for NGC 4569 and NGC 4826, and $\sim 100 M_\odot pc^{-2}$ for NGC 3627. In the first two, mean Σ_{H_2} are 20–40 times higher so the neglect of H_I will introduce a few percent systematic underestimate of gas surface density; nevertheless, the H_I beam is large so this could be an underestimate. NGC 3627 has the highest Σ_{H_2} of our sample (600–700 $M_\odot pc^{-2}$), but the dense H_I gas is still a relatively small fraction. In any case, as shown by the model predictions of Krumholz et al. (2009) in Fig. 8, Σ_{H_2} in the NUGA galaxies even at 200 pc resolution are in the surface-density regime where H_2 is expected to dominate.

For most of CO data of our sample it has been possible to combine interferometric data have been combined with single-dish ones, allowing to resolve the “missing flux” problem (see Table 2). Because in a interferometer two antennas can not be placed closer than some minimum distance (D_{min}), signals larger than some size ($\propto \lambda/D_{min}$) will be attenuated. For only interferometric ^{12}CO maps the spatially extended sources can therefore not be detected, which would have the effect of underestimating the gas surface density.

6.2. Derivation of Σ_{SFR} : diffuse $H\alpha$, $[N II]$ contamination, and $H\alpha$ extinction

Our values of Σ_{SFR} inferred from $H\alpha$ would be overestimated were some fraction of the emission diffuse, not directly associated with ionization by massive stars. Rahman et al. (2011) find that K-S slopes are steeper the larger the fraction of diffuse emission in the SFR tracer (see also Liu et al. 2011). However, they also conclude that diffuse emission either in the SFR tracer or in CO do not compromise results in the high column density regions of the galaxy they studied, NGC 4254. Since NGC 4254 has peak $\Sigma_{H_2} \lesssim 200 M_\odot pc^{-2}$, comparable to the mean Σ_{H_2} of our sample galaxies, we do not expect the potential overestimate of SFR from diffuse $H\alpha$ emission to be a significant problem.

We removed the $[N II]$ contamination within the filter bandpass using average $[N II]/H\alpha$ values available in literature, as typically done in narrow-band studies. However, Blanc et al. (2009), using integral-field spectroscopy to study the spatially-resolved SF relation in NGC 5194, has checked the validity of the assumption of a constant $[N II]/H\alpha$ and the bias introduced by it. They found an increasing $[N II]/H\alpha$ ratio as one goes to fainter $H\alpha$ fluxes, consistent with the nebular emission in the faintest parts of the galaxy (mainly in the inter-arm regions) being dominated by the diffuse ionized gas. Assuming a constant $[N II]/H\alpha$ may thus introduce an underestimation of the $H\alpha$ flux (and therefore of the derived SFR) in the galaxy central regions.

In Sections 1 and 3.3, we have stressed that the $H\alpha$ emission lines are subject to extinction within the galaxies, which we have taken into account for our analysis by adopting $A_V(int)$ values determined for each sample galaxy rather than a mean value. However, we applied this globally, as suggested by Kennicutt & Kent (1983); this is somewhat of an oversimplification because central regions of galaxies are generally subject

to larger extinction than disk regions. This may cause the extinction correction and (therefore) the SFR to be underestimated.

6.3. Choice of the fitting method

A central component of observational investigations is also the quantification of the correlation between two or more observed quantities. Typically, linear regression provides estimates of the zero-point and slope of the “best-fit” regression line between the observed data. Since each adopted methodology to fit a power law to the data introduces a bias in the results, it is important to understand the limitations of common fitting methods. Usually in the K-S relation studies a linear regression in logarithmic space is performed, but methods differ in the treatment of error bars. Some works (e.g., Kennicutt et al. 2007; Rahman et al. 2011; Momose et al. 2013) used the FITEXY algorithm (Press et al. 1989), which has the advantage of incorporating errors in both the ordinate and abscissa coordinates, thus providing a robust regression results, although errors must be assumed to be symmetric in logarithmic space, which is not always the case. Other studies, already quoted in Sect. 3.7 and including the present work, adopted the OLS bisector method, which returns a bisector line in x - and y -axes without the errors taken into account. Both methods have the disadvantage of not being able to incorporate upper limits in the minimization.

For this reason, Blanc et al. (2009) introduced and used a new method for fitting, based on Monte Carlo approach combined with two-dimensional distribution comparison techniques, which is not affected by the above issue. This method has the great advantage to include the regions not detected in the CO map including those with negative measured fluxes, in addition to incorporate the intrinsic scatter in the SF relation as a free parameter and to perform the fitting in linear space avoiding the assumption of log-normal symmetric errors. For a detailed discussion on disadvantages of the linear regressions with respect to a Monte Carlo fitting method for a more realistic treatment of systematics and accurate determination of the parameters and errors, we refer to Blanc et al. (2009) and Shetty et al. (2013). Such an analysis is beyond the scope of this paper.

Based on the IRAM PdBI CO data reduction performed for all NUGA galaxies, we preferred to take into account only data above 3σ level, for which we are sure of the interferometric significance. Momose et al. (2013), analyzing the SF relation at sub-kpc scales of ten nearby galaxies, noted that the choice of CO threshold surface density (3σ also in their case) affects little the results, however repeating the analysis with various thresholds they obtained the same findings in terms of K-S relation. Since we compared our results with Bigiel et al. (2008) (see Fig. 8) who used the OLS bisector method we also adopted it.

We note that results derived from the robust regression fitting method can differ very much from OLS bisector ones (see Table 4) confirming that the choice of the fitting method affects the findings (Blanc et al. 2009; Shetty et al. 2013). This reinforces further the need to compare K-S relation results obtained based on the same fitting method.

7. Conclusions

We have investigated the resolved molecular K-S relation in the central kpc of four NUGA galaxies, of different types, interacting or not, barred or not, with a Seyfert or Liner nucleus. Their SFR ranges from ~ 0.7 to $\sim 4 M_\odot yr^{-1}$, and sSFR from 0.04 to $0.5 Gyr^{-1}$. The spatial scales studied in this work lie between

~20 and 200 pc, and densities sampled are higher than in the usual galaxy disks, extending toward 100–1000 $M_{\odot} \text{pc}^{-2}$.

The first result is that each galaxy has its own molecular SF relation at investigated spatial scales. The K-S relation are most often under-linear (see NGC 4569), with slopes ranging from ~0.5 to ~1.3. The derived depletion time scales range between 1 and 2 Gyr, quite compatible with what is found at larger scale in the COLD GASS sample of nearby galaxies. These results are valid whatever the ^{12}CO line observed, from the (1–0) to (3–2) transition. We also found that the K-S relation changes behavior at spatial scales of ~80–100 pc, with the index N_{fit} starting to sharply decrease with finer resolution with respect to larger scales. However, although a break of the relation between Σ_{H_2} and Σ_{SFR} is expected at small scales (~10–50 pc), due to phenomena such as star formation feedback, life-time of clouds, turbulent cascade, or magnetic fields (e.g., Kruijssen et al. 2014), and it has been observed in M 51 (Liu et al. 2011) and M 33 (Onodera et al. 2010), in dense nuclei as those available thanks to NUGA sample a net break is still not visible at scales of ~20 pc. This might be due to the higher density of GMCs present in galaxy centers, which have to resist higher shear forces. Finally, one of the most important findings is that the proportionality between Σ_{H_2} and Σ_{SFR} found between 10 and 100 $M_{\odot} \text{pc}^{-2}$ is continued at densities as high as $\sim 10^3 M_{\odot} \text{pc}^{-2}$. However, with a common conversion factor, the central regions of the NUGA galaxies have higher Σ_{SFR} for a given gas column than those expected from the models, with a behavior between the mergers/high- z starburst systems and the more quiescent SFGs, assuming that the former require a lower value of α_{CO} .

Acknowledgements. We thank the anonymous referee for useful comments and suggestions which improved the quality of the manuscript. We also thank Daniela Calzetti for precious comments and suggestions. V. Casasola also wishes to thank Laura Magrini and Jacopo Fritz for helpful discussions on star-formation processes. This research has made use of the NASA/IPAC Extragalactic Database (NED) which is operated by the Jet Propulsion Laboratory, California Institute of Technology, under contract with the National Aeronautics and Space Administration. This research has also made use of observations made with the NASA/ESA Hubble Space Telescope, and obtained from the Hubble Legacy Archive, which is a collaboration between the Space Telescope Science Institute (STScI/NASA), the Space Telescope European Coordinating Facility (ST-ECF/ESA) and the Canadian Astronomy Data Centre (CAD/C/NRC/CSA).

References

- Baker, A. J., Jøgee, S., Sakamoto, K., & Scoville, N. Z. 2003, *Active Galactic Nuclei: From Central Engine to Host Galaxy*, 290, 479
- Bigiel, F., Leroy, A., Walter, F., et al. 2008, *AJ*, 136, 2846
- Bigiel, F., Leroy, A., Walter, F., et al. 2010, *AJ*, 140, 1194
- Bigiel, F., Leroy, A. K., Walter, F., et al. 2011, *ApJ*, 730, LL13
- Blanc, G. A., Heiderman, A., Gebhardt, K., Evans, N. J., II, & Adams, J. 2009, *ApJ*, 704, 842
- Boissier, S., Prantzos, N., Boselli, A., & Gavazzi, G. 2003, *MNRAS*, 346, 1215
- Bolatto, A. D., Leroy, A. K., Rosolowsky, E., Walter, F., & Blitz, L. 2008, *ApJ*, 686, 948
- Bolatto, A. D., Wolfire, M., & Leroy, A. K. 2013, *ARA&A*, 51, 207
- Boone, F., Baker, A. J., Schinnerer, E., et al. 2007, *A&A*, 471, 113 (NUGA VII)
- Boone, F., García-Burillo, S., Combes, F., et al. 2011, *A&A*, 525, A18
- Boselli, A., Cortese, L., Boquien, M., et al. 2014, *A&A*, 564, A66
- Bothwell, M. S., Chapman, S. C., Tacconi, L., et al. 2010, *MNRAS*, 405, 219
- Bothwell, M. S., Wagg, J., Ciccone, C., et al. 2014, *MNRAS*, 445, 2599
- Bouché, N., Cresci, G., Davies, R., et al. 2007, *ApJ*, 671, 303
- Braun, R., Walterbos, R. A. M., & Kennicutt, R. C., Jr. 1992, *Nature*, 360, 442
- Braun, R., Walterbos, R. A. M., Kennicutt, R. C., Jr., & Tacconi, L. J. 1994, *ApJ*, 420, 558
- Brinchmann, J., Charlot, S., White, S. D. M., et al. 2004, *MNRAS*, 351, 1151
- Burstein, D., & Heiles, C. 1982, *AJ*, 87, 1165
- Calzetti, D., Kennicutt, R. C., Engelbracht, C. W., et al. 2007, *ApJ*, 666, 870
- Calzetti, D., Wu, S.-Y., Hong, S., et al. 2010, *ApJ*, 714, 1256
- Calzetti, D., Liu, G., & Koda, J. 2012, *ApJ*, 752, 98
- Cardelli, J. A., Clayton, G. C., & Mathis, J. S. 1989, *ApJ*, 345, 245
- Casasola, V., Bettoni, D., & Galletta, G. 2004, *A&A*, 422, 941
- Casasola, V., Hunt, L. K., Combes, F., García-Burillo, S., & Neri, R. 2011, *A&A*, 527, A92 (NUGA XIV)
- Casoli, F., & Gerin, M. 1993, *A&A*, 279, L41
- Chemin, L., Cayatte, V., Balkowski, C., et al. 2003, *A&A*, 405, 89
- Combes, F., García-Burillo, S., Casasola, V., et al. 2013, *A&A*, 558, A124
- Combes, F., García-Burillo, S., Casasola, V., et al. 2014, *A&A*, 565, A97
- Dahlem, M., Heckman, T. M., Fabbiano, G., Lehnert, M. D., & Gilmore, D. 1996, *ApJ*, 461, 724
- Dale, D. A., Cohen, S. A., Johnson, L. C., et al. 2009, *ApJ*, 703, 517
- Dale, D. A., Aniano, G., Engelbracht, C. W., et al. 2012, *ApJ*, 745, 95
- Dame, T. M., Hartmann, D., & Thaddeus, P. 2001, *ApJ*, 547, 792
- Desert, F. X., Bazell, D., & Boulanger, F. 1988, *ApJ*, 334, 815
- de Vaucouleurs, G., de Vaucouleurs, A., Corwin, H. G., Jr., et al. 1991, *Third Reference Catalogue of Bright Galaxies*. Springer, New York, NY (USA), 1991, 2091 p.
- Devereux, N., Taniguchi, Y., Sanders, D. B., Nakai, N., & Young, J. S. 1994, *AJ*, 107, 2006
- Dewangan, G. C., Griffiths, R. E., Di Matteo, T., & Schurch, N. J. 2004, *ApJ*, 607, 788
- Dobbs, C. L., & Pringle, J. E. 2013, *MNRAS*, 432, 653
- Dudik, R. P., Satyapal, S., Gliozzi, M., & Sambruna, R. M. 2005, *ApJ*, 620, 113
- Eales, S. A., Smith, M. W. L., Wilson, C. D., et al. 2010, *A&A*, 518, LL62
- Eracleous, M., Shields, J. C., Chartas, G., & Moran, E. C. 2002, *ApJ*, 565, 108
- Faesi, C. M., Lada, C. J., Forbrich, J., Menten, K. M., & Bouy, H. 2014, *ApJ*, 789, 81
- Feigelson, E. D., & Babu, G. J. 1992, *ApJ*, 397, 55
- Ford, G. P., Gear, W. K., Smith, M. W. L., et al. 2013, *ApJ*, 769, 55
- Fox, J., *Applied regression analysis, linear models, and related models*. Thousand Oaks, CA: Sage publications.
- Gao, Y., & Solomon, P. M. 2004, *ApJS*, 152, 63
- García-Burillo, S., Combes, F., Hunt, L. K., et al. 2003, *A&A*, 407, 485 (NUGA I)
- García-Burillo, S., Combes, F., Schinnerer, E., Boone, F., & Hunt, L. K. 2005, *A&A*, 441, 1011 (NUGA IV)
- García-Burillo, S., Fernández-García, S., Combes, F., et al. 2009, *A&A*, 496, 85 (NUGA XI)
- García-Burillo, S., Usero, A., Alonso-Herrero, A., et al. 2012, *A&A*, 539, AA8
- García-Burillo, S., Combes, F., Usero, A., et al. 2014, *A&A*, 567, AA125
- Garn, T., & Best, P. N. 2010, *MNRAS*, 409, 421
- Genzel, R., Tacconi, L. J., Gracia-Carpio, J., et al. 2010, *MNRAS*, 407, 2091
- Glover, S. C. O., & Mac Low, M.-M. 2011, *MNRAS*, 412, 337
- Guibert, J., Lequeux, J., & Viallefond, F. 1978, *A&A*, 68, 1
- Guilloteau, S., & Lucas, R. 2000, *Imaging at Radio through Submillimeter Wavelengths*, 217, 299
- Haan, S., Schinnerer, E., Mundell, C. G., García-Burillo, S., & Combes, F. 2008, *AJ*, 135, 232
- Haan, S., Schinnerer, E., Emsellem, E., et al. 2009, *ApJ*, 692, 1623
- Helfer, T. T., Thornley, M. D., Regan, M. W., et al. 2003, *ApJS*, 145, 259
- Hernández-García, L., González-Martín, O., Márquez, I., & Masegosa, J. 2013, *A&A*, 556, AA47
- Ho, L. C., Filippenko, A. V., Sargent, W. L. W., & Peng, C. Y. 1997, *ApJS*, 112, 391
- Ho, L. C. 1999, *ApJ*, 516, 672
- Ho, L. C., Feigelson, E. D., Townsley, L. K., et al. 2001, *ApJ*, 549, L51
- Ho, L. C., & Ulvestad, J. S. 2001, *ApJS*, 133, 77
- Hummel, E., van der Hulst, J. M., Keel, W. C., & Kennicutt, R. C., Jr. 1987, *A&A*, 70, 517
- Ihaka, R., & Gentleman, R. 1996, *J. Comput. Graph. Stat.*, 5, 299
- Iono, D., Wilson, C. D., Yun, M. S., et al. 2009, *ApJ*, 695, 1537
- Isobe, T., Feigelson, E. D., Akritas, M. G., & Babu, G. J. 1990, *ApJ*, 364, 104
- Israel, F. P. 2009, *A&A*, 493, 525
- Jøgee, S., Scoville, N., & Kenney, J. D. P. 2005, *ApJ*, 630, 837
- Kennicutt, R. C., Jr., & Kent, S. M. 1983, *AJ*, 88, 1094
- Kennicutt, R. C., Jr. 1989,
- Kennicutt, R. C., Jr. 1992, *ApJ*, 388, 310
- Kennicutt, R. C., Jr. 1998a, *ARA&A*, 36, 189
- Kennicutt, R. C., Jr. 1998b, *ApJ*, 498, 541
- Kennicutt, R. C., Jr., Armus, L., Bendo, G., et al. 2003, *PASP*, 115, 928
- Kennicutt, R. C., Jr., Calzetti, D., Walter, F., et al. 2007, *ApJ*, 671, 333
- Kennicutt, R. C., Jr., Lee, J. C., Funes, S. J., José G., Sakai, S., & Akiyama, S. 2008, *ApJS*, 178, 247
- Kennicutt, R. C., Jr., Hao, C.-N., Calzetti, D., et al. 2009, *ApJ*, 703, 1672
- Kennicutt, R. C., Calzetti, D., Aniano, G., et al. 2011, *PASP*, 123, 1347
- Kennicutt, R. C., & Evans, N. J. 2012, *ARA&A*, 50, 531
- Koda, J., Scoville, N., Hasegawa, T., et al. 2012, *ApJ*, 761, 41
- Komugi, S., Sofue, Y., Nakanishi, H., Onodera, S., & Egusa, F. 2005, *PASJ*, 57, 733
- Komugi, S., Kohno, K., Tosaki, T., et al. 2007, *PASJ*, 59, 55
- Krips, M., Eckart, A., Krichbaum, T. P., et al. 2007, *A&A*, 464, 553

- Krips, M., Neri, R., García-Burillo, S., et al. 2008, *ApJ*, 677, 262
- Krips, M., Martín, S., Eckart, A., et al. 2011, *ApJ*, 736, 37
- Kroupa, P. 2001, *MNRAS*, 322, 231
- Kruijjssen, J. M. D., Longmore, S. N., Elmegreen, B. G., et al. 2014, *MNRAS*, 440, 3370
- Krumholz, M. R., & McKee, C. F. 2005, *ApJ*, 630, 250
- Krumholz, M. R., & Thompson, T. A. 2007, *ApJ*, 669, 289
- Krumholz, M. R., McKee, C. F., & Tumlinson, J. 2009, *ApJ*, 699, 850
- Krumholz, M. R., Dekel, A., & McKee, C. F. 2012, *ApJ*, 745, 69
- Lada, C. J., Lombardi, M., & Alves, J. F. 2010, *ApJ*, 724, 687
- Lanz, L., Zezas, A., Brassington, N., et al. 2013, *ApJ*, 768, 90
- Laurikainen, E., & Salo, H. 2002, *MNRAS*, 337, 1118
- Lebrun, F., Bennett, K., Bignami, G. F., et al. 1983, *ApJ*, 274, 231
- Leroy, A. K., Walter, F., Brinks, E., et al. 2008, *AJ*, 136, 2782
- Leroy, A. K., Walter, F., Bigiel, F., et al. 2009, *AJ*, 137, 4670
- Leroy, A. K., Walter, F., Sandstrom, K., et al. 2013, *AJ*, 146, 19
- Li, G. K., Robust regression. In *Exploring Data Tables, Trends, and Shapes*, ed. D. C. Hoaglin, F. Mosteller, and J. W. Tukey, Wiley
- Lindt-Krieg, E., Eckart, A., Neri, R., et al. 2008, *A&A*, 479, 377
- Liu, G., Koda, J., Calzetti, D., Fukuhara, M., & Momose, R. 2011, *ApJ*, 735, 63
- Madore, B. F. 1977, *MNRAS*, 178, 1
- Magrini, L., Bianchi, S., Corbelli, E., et al. 2011, *A&A*, 535, A13
- Maloney, P., & Black, J. H. 1988, *ApJ*, 325, 389
- Mao, R.-Q., Schulz, A., Henkel, C., et al. 2010, *ApJ*, 724, 1336
- Matsushita, S., Sakamoto, K., Kuo, C.-Y., et al. 2004, *ApJ*, 616, L55
- Mauersberger, R., Henkel, C., Walsh, W., & Schulz, A. 1999, *A&A*, 341, 256
- McKee, C. F., & Ostriker, E. C. 2007, *ARA&A*, 45, 565
- Momose, R., Koda, J., Kennicutt, R. C., Jr., et al. 2013, *ApJ*, 772, L13
- Moustakas, J., Kennicutt, R. C., Jr., Tremonti, C. A., et al. 2010, *ApJS*, 190, 233
- Muraoka, K., Kohno, K., Tosaki, T., et al. 2007, *PASJ*, 59, 43
- Nakanishi, H., Sofue, Y., & Koda, J. 2005, *PASJ*, 57, 905
- Narayanan, D., Cox, T. J., Shirley, Y., et al. 2008, *ApJ*, 684, 996
- Narayanan, D., Krumholz, M. R., Ostriker, E. C., & Hernquist, L. 2012, *MNRAS*, 421, 3127
- Oka, T., Hasegawa, T., Sato, F., et al. 2001, *ApJ*, 562, 348
- Onodera, S., Kuno, N., Tosaki, T., et al. 2010, *ApJ*, 722, L127
- Paladino, R., Murgia, M., Tarchi, A., Moscadelli, L., & Comito, C. 2008, *A&A*, 485, 679
- Pogge, R. W., Maoz, D., Ho, L. C., & Eracleous, M. 2000, *ApJ*, 532, 323
- Press, W. H., Flannery, B. P., Teukolsky, S. A., & Vetterling, W. T. 1989, Cambridge: University Press, |c1989,
- Ptak, A., Colbert, E., van der Marel, R. P., et al. 2006, *ApJS*, 166, 154
- Quirk, W. J. 1972, *ApJ*, 176, L9
- Rahman, N., Bolatto, A. D., Wong, T., et al. 2011, *ApJ*, 730, 72
- Rahman, N., Bolatto, A. D., Xue, R., et al. 2012, *ApJ*, 745, 183
- Regan, M. W., Thornley, M. D., Helfer, T. T., et al. 2001, *ApJ*, 561, 218
- Riechers, D. A., Walter, F., Carilli, C. L., & Bertoldi, F. 2007, *ApJ*, 671, L13
- Rieke, G. H., Alonso-Herrero, A., Weiner, B. J., et al. 2009, *ApJ*, 692, 556
- Rix, H.-W. R., Kennicutt, R. C., Jr., Braun, R., & Walterbos, R. A. M. 1995, *ApJ*, 438, 155
- Rosolowsky, E., & Blitz, L. 2005, *ApJ*, 623, 826
- Saintonge, A., Kauffmann, G., Wang, J., et al. 2011, *MNRAS*, 415, 61
- Sakamoto, S., Hasegawa, T., Hayashi, M., Handa, T., & Oka, T. 1995, *ApJS*, 100, 125
- Sakamoto, K., Okumura, S. K., Ishizuki, S., & Scoville, N. Z. 1999, *ApJS*, 124, 403
- Sandstrom, K. M., Leroy, A. K., Walter, F., et al. 2013, *ApJ*, 777, 5
- Sawada, T., Hasegawa, T., Handa, T., et al. 2001, *ApJS*, 136, 189
- Schlegel, D. J., Finkbeiner, D. P., & Davis, M. 1998, *ApJ*, 500, 525
- Schmidt, M. 1959, *ApJ*, 129, 243
- Schmidt, M. 1963, *ApJ*, 137, 758
- Schruba, A., Leroy, A. K., Walter, F., Sandstrom, K., & Rosolowsky, E. 2010, *ApJ*, 722, 1699
- Schruba, A., Leroy, A. K., Walter, F., et al. 2011, *AJ*, 142, 37
- Schuster, K. F., Kramer, C., Hitschfeld, M., Garcia-Burillo, S., & Mookerjee, B. 2007, *A&A*, 461, 143
- Scoville, N., & Young, J. S. 1983, *ApJ*, 265, 148
- Scoville, N. Z., Yun, M. S., Sanders, D. B., Clemens, D. P., & Waller, W. H. 1987, *ApJS*, 63, 821
- Scoville, N. Z., Polletta, M., Ewald, S., et al. 2001, *AJ*, 122, 3017
- Shetty, R., Kelly, B. C., & Bigiel, F. 2013, *MNRAS*, 430, 288
- Shetty, R., Kelly, B. C., Rahman, N., et al. 2014, *MNRAS*, 437, L61
- Shetty, R., Clark, P. C., & Klessen, R. S. 2014, *MNRAS*, 442, 2208
- Skibba, R. A., Engelbracht, C. W., Dale, D., et al. 2011, *ApJ*, 738, 89
- Smith, B. J., Harvey, P. M., Colome, C., et al. 1994, *ApJ*, 425, 91
- Sofue, Y., Koda, J., Nakanishi, H., & Onodera, S. 2003, *PASJ*, 55, 59
- Solomon, P. M., Barrett, J., Sanders, D. B., & de Zafra, R. 1983, *ApJ*, 266, L103
- Solomon, P. M., Rivolo, A. R., Barrett, J., & Yahil, A. 1987, *ApJ*, 319, 730
- Solomon, P. M., & Barrett, J. W. 1991, *Dynamics of Galaxies and Their Molecular Cloud Distributions*, 146, 235
- Solomon, P. M., Downes, D., Radford, S. J. E., & Barrett, J. W. 1997, *ApJ*, 478, 144
- Springel, V., & Hernquist, L. 2003, *MNRAS*, 339, 289
- Strong, A. W., Bloemen, J. B. G. M., Dame, T. M., et al. 1988, *A&A*, 207, 1
- Tacconi, L. J., & Young, J. S. 1990, *ApJ*, 352, 595
- Tan, J. C., Silk, J., & Bland, C. 1999, *ApJ*, 522, 579
- Terashima, Y., Ho, L. C., Ptak, A. F., et al. 2000, *ApJ*, 535, L79
- Thilker, D. A., Boissier, S., Bianchi, L., et al. 2007, *ApJS*, 173, 572
- Ulvestad, J. S., & Ho, L. C. 2001, *ApJ*, 562, L133
- Urbanik, M., Graeve, R., & Klein, U. 1985, *A&A*, 152, 291
- Verley, S., Corbelli, E., Giovanardi, C., & Hunt, L. K. 2010, *A&A*, 510, A64
- Viaene, S., Fritz, J., Baes, M., et al. 2014, arXiv:1403.4272
- Vlahakis, C., van der Werf, P., Israel, F. P., & Tilanus, R. P. J. 2013, *MNRAS*, 433, 1837
- Vutisalchavakul, N., Evans, N. J., II, & Battersby, C. 2014, *ApJ*, 797, 77
- Walter, F., Brinks, E., de Blok, W. J. G., et al. 2008, *AJ*, 136, 2563
- Watanabe, Y., Sorai, K., Kuno, N., & Habe, A. 2011, *MNRAS*, 411, 1409
- Wilson, C. D., Warren, B. E., Israel, F. P., et al. 2009, *ApJ*, 693, 1736
- Wilson, C. D., Warren, B. E., Israel, F. P., et al. 2012, *MNRAS*, 424, 3050
- Wong, T., & Blitz, L. 2002, *ApJ*, 569, 157
- Wu, H., Cao, C., Hao, C.-N., et al. 2005, *ApJ*, 632, L79
- Young, J. S., & Scoville, N. 1982, *ApJ*, 258, 467
- Zhou, Z.-M., Cao, C., Meng, X.-M., & Wu, H. 2011, *AJ*, 142, 38
- Zhu, Y.-N., Wu, H., Cao, C., & Li, H.-N. 2008, *ApJ*, 686, 155